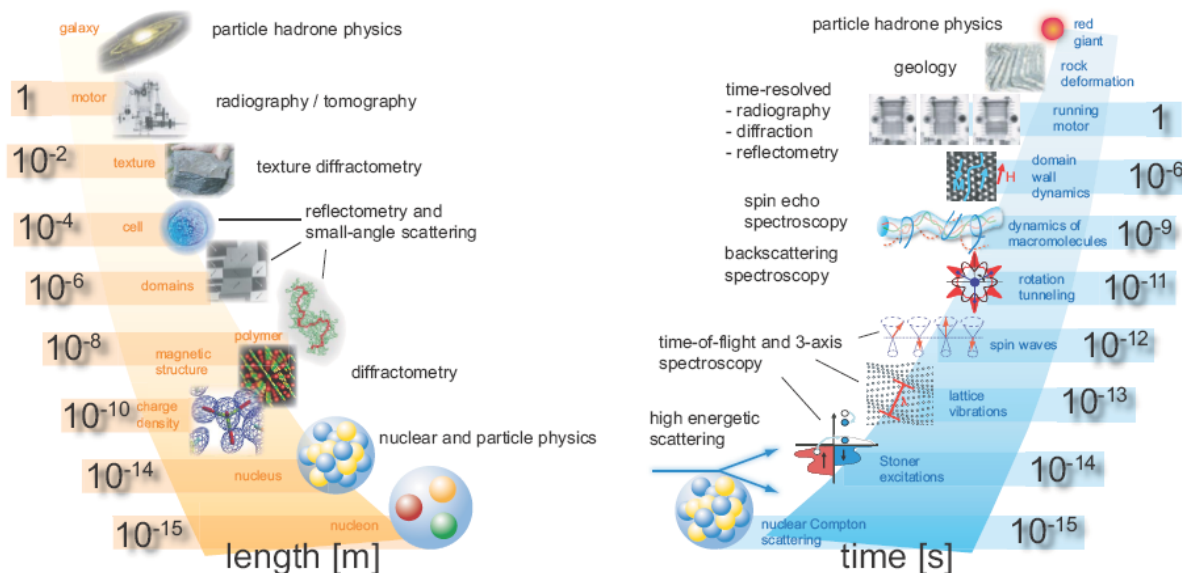


## 5. Applications of neutron scattering

Thomas Brückel, IFF, Forschungszentrum Jülich

### 5.1 Introduction



**Fig 5.1:** Length- and time scales covered by research with neutrons giving examples for applications and neutron techniques [1].

Research with neutrons covers an extraordinary range of length- and time scales as depicted in figure 5.1. The very extremes of length scales - below  $10^{-12}$  m - are the domain of nuclear and particle physics, where e. g. measurements of the charge or electric dipole moment of the neutron provide stringent tests of the standard model of particle physics without the need of huge and costly accelerators. On the other extreme, neutrons also provide information on length- and time scales relevant for astronomical dimensions, e. g. the decay series of radioactive isotopes produced by neutron bombardment give information on the creation of elements in the early universe. In this course, however, we are only concerned with neutrons as a probe for condensed matter research and therefore restrict ourselves to a discussion of neutron scattering. Still, the various neutron scattering techniques cover an area in phase space from picometers pm up to meters and femtoseconds fs up to hours, a range, which probably no other probe can cover to such an extend.

Different specialized neutron scattering techniques are required to obtain structural information on different length scales:

- With *wide angle neutron diffractometry*, magnetization densities can be determined within single atoms on a length scale of ca.  $10$  pm<sup>1</sup>. The position of atoms can be determined on a similar length scale, while distances between atoms lie in the  $0.1$  nm range<sup>2</sup>.

<sup>1</sup> In this sense, neutrons are not only nanometer nm, but even picometer pm probes!

<sup>2</sup> In what follows, we use as “natural atomic unit” the Ångström, with  $1 \text{ \AA} = 0.1 \text{ nm}$ .

- The sizes of large macromolecules, magnetic domains or biological cells lie in the range of nm to  $\mu\text{m}$  or even mm. For such studies of large scale structures, one applies *reflectometry* or *small angle scattering* techniques.
- Most materials relevant for engineering or geo-science occur neither in form of single crystals, nor in form of fine powders. Instead they have a grainy structure, often with preferred orientation of the grains. This so called texture determines the macroscopic strength of the material along different directions. *Texture diffractometry* as a specialized technique allows one to determine this grainy structure on length scales of up to mm.
- Finally, for even larger structures, one uses imaging techniques, such as neutron *radiography* or *tomography*, which give a 2dimensional projection or full 3-dimensional view into the interior of a sample due to the attenuation of the neutron beam, the phase shift or other contrast mechanisms.

In a similar way, different specialized neutron scattering techniques are required to obtain information on the system's dynamics on different time scales:

- *Neutron Compton scattering*, where a high energy neutron in the eV energy range makes a deep inelastic collision with a nucleus in so-called impulse approximation, gives us the momentum distribution of the atoms within the solid. Interaction times are in the femtosecond fs time range.
- In magnetic metals, there exist single particle magnetic excitations, so-called Stoner excitations, which can be observed with inelastic scattering of high energy neutrons using the so-called *time-of-flight spectroscopy* or the *triple axis spectroscopy* technique. Typically, these processes range from fs to several hundred fs.
- Lattice vibrations (phonons) or spin waves in magnetic systems (magnons) have frequencies in the picosecond ps time range. Again these excitations can be observed with *time-of-flight* or *triple axis spectroscopy*.
- Slower processes in condensed matter are the tunneling of atoms, for example in molecular crystals or the slow dynamics of macromolecules. Characteristic time scales for these processes lie in the nanosecond ns time range. They can be observed with specialized techniques such as *backscattering spectroscopy* or *spin-echo spectroscopy*.
- Even slower processes occur in condensed matter on an ever increasing range of length scales. One example is the growth of domains in magnetic systems, where domain walls are pinned by impurities. These processes may occur with typical time constants of microseconds  $\mu\text{s}$ . Periodic processes on such time scales can be observed with *stroboscopic neutron scattering* techniques.
- Finally, *kinematic neutron scattering* or imaging techniques, where data is taken in consecutive time slots, allow one to observe processes from the millisecond ms to the hour h range.

In this chapter, we will overview the various techniques used in neutron scattering and provide some examples for their application. We will start by repeating the properties of the different correlation functions, in order to be able to judge what kind of information we can obtain from a certain neutron scattering experiment. We will introduce neutron scattering techniques used to obtain information on “where the atoms are” (diffractometry) and “what the atoms do” (spectroscopy). We will finish by reviewing the range of applicability of various neutron scattering methods and compare them to other experimental techniques.

## 5.2 Scattering and correlation functions

In the chapter on “Correlation Functions” it has been shown that the neutron scattering cross section for nuclear scattering can be expressed in the following form (for simplicity, we restrict ourselves to a mono-atomic system):

$$\frac{\partial^2 \sigma}{\partial \Omega \partial \omega} = \frac{k'}{k} \cdot N \cdot \left[ \left( \overline{|b|^2} - |\bar{b}|^2 \right) S_{inc}(\underline{Q}, \omega) + |\bar{b}|^2 S_{coh}(\underline{Q}, \omega) \right] \quad (5.1)$$

The cross section is proportional to the number  $N$  of atoms. It contains a kinematical factor  $k'/k$ , i. e. the magnitude of the final wave vector versus the magnitude of the incident wave vector, which results from the phase-space density. The scattering cross section contains two summands: one is the coherent scattering cross section, which depends on the magnitude square of the average scattering length density  $|\bar{b}|^2$  and the other one is the incoherent scattering, which depends on the variance of the scattering length  $\left( \overline{|b|^2} - |\bar{b}|^2 \right)$ . The cross section (5.1) has a very convenient form: it separates the interaction strength between probe (the neutrons) and sample from the properties of the system studied. The latter is given by the so-called scattering functions  $S_{coh}(\underline{Q}, \omega)$  and  $S_{inc}(\underline{Q}, \omega)$ , which are completely independent of the probe and a pure property of the system under investigation [2]. The *coherent scattering function*  $S_{coh}(\underline{Q}, \omega)$  (also called *dynamical structure factor* or *scattering law*) is a Fourier transform in space and time of the pair correlation function:

$$S_{coh}(\underline{Q}, \omega) = \frac{1}{2\pi\hbar} \int G(\underline{r}, t) e^{i(\underline{Q}\cdot\underline{r} - \omega t)} d^3 r dt \quad (5.2)$$

Here the *pair correlation function*  $G(\underline{r}, t)$  depends on the time dependent positions of the atoms in the sample:

$$\begin{aligned} G(\underline{r}, t) &= \frac{1}{N} \sum_{ij} \int \langle \delta(\underline{r}' - \underline{r}_i(0)) \cdot \delta(\underline{r}' + \underline{r} - \underline{r}_j(t)) \rangle d^3 r' \\ &= \frac{1}{N} \int \langle \rho(\underline{r}', 0) \cdot \rho(\underline{r}' + \underline{r}, t) \rangle d^3 r' \end{aligned} \quad (5.3)$$

$\underline{r}_i(0)$  denotes the position of atom  $i$  at time 0, while  $\underline{r}_j(t)$  denotes the position of another atom  $j$  at time  $t$ . The angle brackets denote the thermodynamic ensemble average, the integral extends over the entire sample volume and the sum runs over all atom pairs in the sample. Instead of correlating the positions of two point-like scatterers at different times, one can rewrite the pair correlation function in terms of the particle density as given in the second line of (5.3). Coherent scattering arises from the superposition of the amplitudes of waves scattered from one particle at time  $0$  and a second particle at time  $t$ , averaged over the entire sample volume and the thermodynamic state of the sample. In contrast, incoherent scattering arises from the superposition of waves scattered from the same particle at different times. Therefore the *incoherent scattering function*  $S_{inc}(\underline{Q}, \omega)$  is given in the following form:

$$S_{inc}(\underline{Q}, \omega) = \frac{1}{2\pi\hbar} \int G_s(\underline{r}, t) e^{i(\underline{Q}\cdot\underline{r} - \omega t)} d^3 r dt \quad (5.4)$$

which is the Fourier transform in space and time of the *self correlation function*  $G_s(\underline{r}, t)$ :

$$G_s(\underline{r}, t) = \frac{1}{N} \sum_j \int \langle \delta(\underline{r}' - \underline{r}_j(0)) \cdot \delta(\underline{r}' + \underline{r} - \underline{r}_j(t)) \rangle d^3 r' \quad (5.5)$$

We next define the *intermediate scattering function*  $S(\underline{Q}, t)$  as the purely spatial Fourier transform of the correlation function (here we have dropped the index “coh” and “inc”, re-

spectively, as the intermediate scattering function can be defined for coherent as well as for incoherent scattering in the same way):

$$\begin{aligned} S(\underline{Q}, t) &:= \int G(\underline{r}, t) e^{i\underline{Q}\cdot\underline{r}} d^3r \\ &= S(\underline{Q}, \infty) + S'(\underline{Q}, t) \end{aligned} \quad (5.6)$$

For reasons, which will become apparent below, we have separated in the second line the intermediate scattering function for infinite time

$$S(\underline{Q}, \infty) = \lim_{t \rightarrow \infty} S(\underline{Q}, t) \quad (5.7)$$

from the time development at intermediate times. Given this form of the intermediate scattering function  $S(\underline{Q}, t)$ , we can now calculate the scattering function as the temporal Fourier transform of the intermediate scattering function:

$$\begin{aligned} S(\underline{Q}, \omega) &= \frac{1}{2\pi\hbar} \int_{-\infty}^{+\infty} S(\underline{Q}, t) e^{-i\omega t} dt = \frac{1}{2\pi\hbar} \int_{-\infty}^{+\infty} [S(\underline{Q}, \infty) + S'(\underline{Q}, t)] e^{-i\omega t} dt \\ &= \underbrace{\frac{1}{\hbar} \delta(\omega) S(\underline{Q}, \infty)}_{\text{elastic scattering}} + \underbrace{\frac{1}{2\pi\hbar} \int_{-\infty}^{+\infty} S'(\underline{Q}, t) e^{-i\omega t} dt}_{\text{inelastic scattering}} \end{aligned} \quad (5.8)$$

In this way, the scattering function has been separated into one term for frequency 0, i. e. vanishing energy transfer  $\Delta E = \hbar\omega = 0$  and one term for non-vanishing energy transfer. The first term is the purely elastic scattering, which is given by the correlation function at infinite times. Correlation at infinite times is obtained for particles at rest. A prominent example is the Bragg scattering from a crystalline material, which is purely elastic, while the scattering from liquids is purely inelastic, since the atoms in liquids are moving around freely and thus the correlation function vanishes in the limit of infinite time differences.

Often times the energy of the scattered neutron is not discriminated in the detector. In such experiments, where the detector is set at a given scattering angle, but does not resolve the energies of the scattered neutrons, we measure an *integral cross section* for a fixed direction  $\hat{k}'$  of  $\underline{k}'$ :

$$\left( \frac{d\sigma}{d\Omega} \right)_{\text{coh, int}} = \int \frac{\partial^2 \sigma}{\partial \Omega \partial \omega} \Big|_{\hat{k}' = \text{const}} \cdot d\omega \quad (5.9)$$

Momentum and energy conservation are expressed by the following kinematic equations of scattering:

$$\underline{Q} = \underline{k}' - \underline{k} \quad ; \quad \hbar\omega = E - E' = \frac{\hbar^2}{2m} (k^2 - k'^2) \quad (5.10)$$

Due to these kinematic conditions, the scattering vector  $\underline{Q}$  will vary with the energy of the scattered neutron  $E'$  or the energy transfer  $\hbar\omega$  as the integral in (5.9) is performed. The so-called *quasi-static approximation* neglects this variation and uses the scattering vector  $\underline{Q}_0$  for elastic scattering ( $\hbar\omega = 0$ ) in (5.9). This approximation is valid only if the energy transfer is small compared to the initial energy. This means that the movements of the atoms are negligible during the propagation of the radiation wave front from one atom to the other. In this case, the above integral can be approximated as follows:

$$\begin{aligned} \left( \frac{d\sigma}{d\Omega} \right)_{\text{coh, QSA}} &= \frac{k'}{k} \frac{N}{2\pi\hbar} \int \left( \int G(\underline{r}, t) e^{i(\underline{Q}_0 \cdot \underline{r} - \omega t)} d^3r dt \right) d\omega \\ &= \frac{k'}{k} \frac{N}{2\pi\hbar} \int G(\underline{r}, t) e^{i\underline{Q}_0 \cdot \underline{r}} \delta(t) d^3r dt = \frac{k'}{k} \frac{N}{2\pi\hbar} \int G(\underline{r}, 0) e^{i\underline{Q}_0 \cdot \underline{r}} d^3r \end{aligned} \quad (5.11)$$

which shows that the integral scattering in quasi-static approximation depends on the *instantaneous spatial correlation function* only, i. e. it measures a snapshot of the arrangement of atoms within the sample. This technique is e. g. very important for the determination of short-range order in liquids, where no elastic scattering occurs (see above).

Our discussion on correlation functions can be summarized in a schematic diagrammatic form, see figure 5.2.

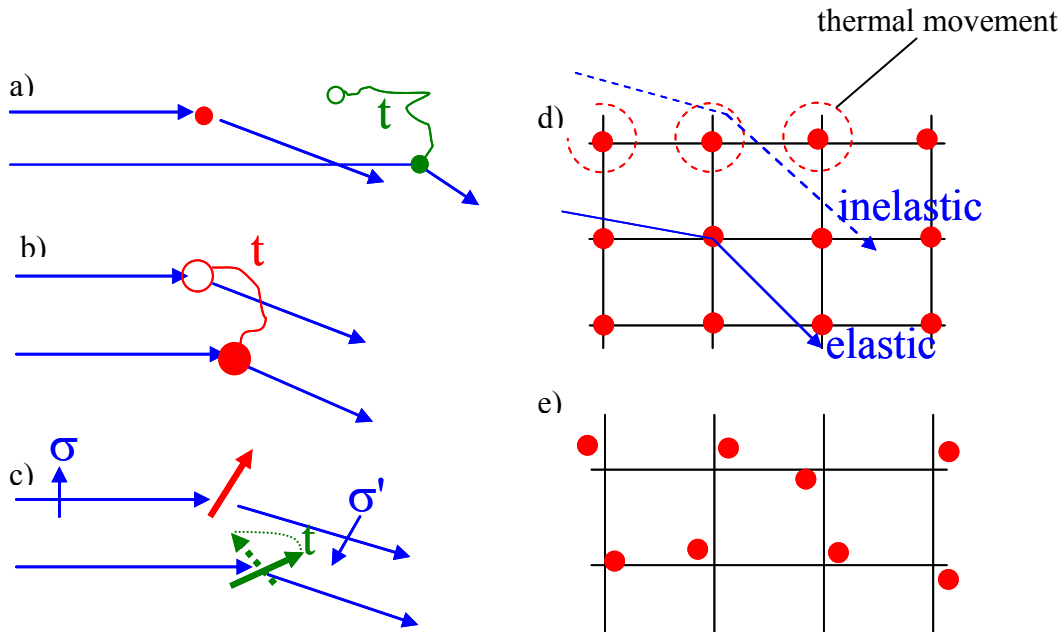


**Fig. 5.2:** Schematic diagrams depicting the various scattering processes: a) coherent scattering is connected with the pair correlation function in space-and time; b) incoherent scattering is connected with the self-correlation function; c) magnetic scattering is connected with the spin pair correlation function; d) elastic and inelastic scattering from a crystal measures average positions and movements of the atoms, respectively, e) inelastic scattering in quasistatic approximation sees a snapshot of the sample.

Figure 5.2 shows that coherent scattering is related to the pair correlation between different atoms at different times (5.2a), while incoherent scattering relates to the one particle self correlation function at different times (5.2b). In analogy to nuclear scattering, magnetic scattering depends on the correlation function between magnetic moments of the atoms. If the magnetic moment is due to spin only, it measures the *spin pair correlation function*. Since the magnetic moment is a vector quantity, this correlation function strongly depends on the neutron polarization. For this reason, in magnetic scattering we often perform a polarization analysis as discussed in the corresponding chapter. Figure 5.2d depicts elastic and inelastic scattering from atoms on a regular lattice. Elastic scattering depends on the infinite time correlation and thus gives us information on the time averaged structure. Excursions of the atoms from their time averaged positions due to the thermal movement will give rise to inelastic scattering, which allows one e. g. to determine the spectrum of lattice vibrations, see chapter on “inelastic neutron scattering”. Finally, an experiment without energy analysis in quasi-static approximation will give us the instantaneous correlations between the atoms, see figure 5.2e. This schematic picture shows a snapshot of the atoms on a regular lattice. Their positions differ from the time averaged positions due to thermal movement.

### 5.3 The generic scattering experiment

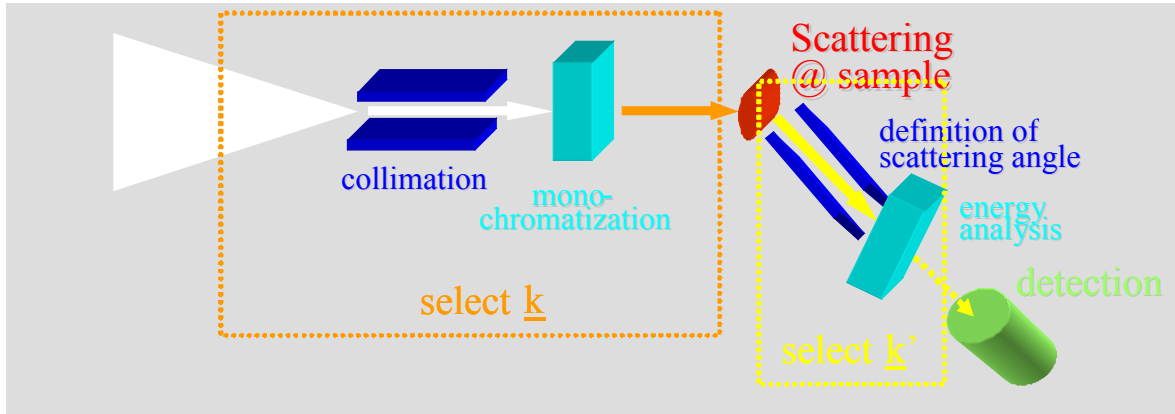


**Fig. 5.3:** Schematic diagram of a generic scattering experiment; the primary spectrometer in front of the sample serves to select an incident wave vector distribution by means of collimation and monochromatization; the secondary spectrometer after the sample selects a final wave vector; the number of neutrons for a given distribution of incident wave vector  $\underline{k}$  and final wave vector  $\underline{k}'$  is counted in the detector.

A generic scattering experiment is depicted schematically in figure 5.3. The incident beam is prepared by collimators, which define the direction of the beam and monochromators, which define the energy of the incident neutrons. Together these optical elements select an incident wave vector  $\underline{k}$ . In reality, since these neutron-optical elements are never perfect, a certain distribution of incident wave vectors around an average wave vector is selected in the primary spectrometer. In an analogous manner, a final wave vector - or better a distribution of final wave vectors - is being selected from all scattered waves after the sample by the secondary spectrometer. Finally the scattered neutrons are being counted in the detector. Since our neutron-optical elements are never perfect, the measured intensity in the detector is not simply proportional to the scattering function  $S(\underline{Q}, \omega)$  (or more precisely, the cross section), but it is proportional to the convolution of the scattering function (or cross section) with the *experimental resolution function*  $R$ :

$$I(\underline{Q}_0, \omega_0) \propto \iint S(\underline{Q}, \omega) R(\underline{Q}_0 - \underline{Q}, \omega_0 - \omega) d^3 Q d\omega \quad (5.12)$$

Here, the resolution function  $R$  appears due to the limited ability of any experimental setup to define an incident or final wave vector  $\underline{k}$  or  $\underline{k}'$ , respectively.  $R$  therefore depends purely on the instrumental parameters and not on the scattering system under investigation. The art of any neutron scattering experiment is to adjust the instrument - and with it the resolution function - to the problem under investigation. If the resolution of the instrument is too tight, the intensity in the detector becomes too small and counting statistics will limit the precision of the measurement. If, however, the resolution is too relaxed, the intensity will be smeared out and will not allow one to determine the scattering function properly.

The simplest way to collimate an incident beam is to put two slits with given openings in a certain distance in the beam path and thus define the angular spread of the incident beam. For monochromatization of a neutron beam, usually one of two different methods is applied:

- One can use the wave property of the neutron and diffract the neutron beam from a single crystal. According to Bragg's law  $2d \sin \theta = \lambda$ , a certain wave length  $\lambda$  is being selected for a given lattice  $d$ -spacing under a scattering angle  $2\theta$ .

- One can use the particle property of the neutron and use the neutron time-of-flight to determine its velocity and thus its kinetic energy. How this is being done technically will be discussed in subsequent chapters.

Following our discussion of the correlation functions, we will now distinguish two principally different types of neutron scattering instruments:

- Diffractometers: these are scattering instruments, which either perform no energy analysis at all, or which measure only the truly elastic scattering. As discussed in chapter 5.2, the truly elastic scattering allows one to determine the time averaged structure. The prominent example is Bragg scattering from single crystals. If, however, no energy analysis is performed, one usually makes sure that one works in quasistatic approximation to facilitate the interpretation of the scattered intensity distribution. Quasistatic approximation corresponds to a snapshot of the scatterers in the sample and is important for example to determine short-range order in a liquid. Be it elastic scattering or integral scattering in quasistatic approximation, a diffraction experiment allows one to determine the position of the scatterers only. The movement of the scatterers is not accessible with such a diffraction experiment. Similarly, in a diffraction experiment for magnetic scattering, the arrangement of magnetic moments within the sample, i. e. its magnetic structure, can be determined, while the spin dynamics is not accessible in a diffraction experiment<sup>3</sup>.
- Spectrometers: a neutron spectrometer is dedicated to measure inelastic scattering, i. e. to determine the change of the neutrons' kinetic energy  $E = \frac{\hbar^2 k^2}{2m}$  during the scattering process. Such an experiment requires the analysis of the energy of the scattered neutrons, in contrast to a conventional diffractometer. Now the intensity measured in the detector depends on momentum- and energy- transfer and is proportional to the convolution of the double differential scattering cross section (5.1) with the resolution function of the instrument (5.12). Therefore a neutron spectrometer gives us information on the scattering functions (coherent or incoherent) and thus on the truly time dependent pair- or self correlation functions. This is why spectrometers are used to determine the dynamics of a system after its structure has been determined in a previous diffraction experiment<sup>4</sup>.

---

<sup>3</sup> In fact there is a way to access also spin- or lattice- dynamics in a diffraction experiment: lattice vibrations will give rise to diffuse scattering around Bragg peaks, so-called thermal diffuse scattering, which can be modelled and thus the spectrum of excitations can be determined in an indirect, but not model-free direct way.

<sup>4</sup> Of course, spectrometers could also be used to determine the structure, but usually their resolution is not at all adapted to this purpose.

## 5.4 Diffractometers

### 5.4.1 Wide angle diffraction versus small angle scattering

According to (5.10), the momentum transfer during a scattering experiment is given by  $\hbar\mathbf{Q} = \hbar\mathbf{k}' - \hbar\mathbf{k}$ . Remembering that  $k = \frac{2\pi}{\lambda}$ , the magnitude of the scattering vector  $Q$  can be expressed in terms of wavelength  $\lambda$  and scattering angle  $2\theta$  as:

$$Q = \frac{4\pi}{\lambda} \sin \theta \quad (5.13)$$

As we have seen in chapter 5.2, the scattering cross section is related to the Fourier transform of the spatial correlation function and therefore a reciprocal relation exists between characteristic real space distances  $d$  and the magnitude of the scattering vector  $Q$ , for which intensity maxima appear:

$$\Delta Q \sim \frac{2\pi}{d} \quad (5.14)$$

Bragg scattering from crystals provides an example for this equation (compare chapter: "A neutron primer"): the distance between maxima of the Laue function is determined by  $\Delta Q \cdot d = 2\pi$ , where  $d$  is the corresponding real space periodicity. Reflectometry provides another example (see below): the  $Q$ -distance between Kiessig fringes is given by the relation  $\Delta Q \cdot d \sim 2\pi$  (compare (5.19)), where  $d$  is the layer thickness.

(5.14) is central for the choice of an instrument or experimental set-up, since it tells us which  $Q$ -range we have to cover in order to get information on a certain length range in real space. (5.13) tells us, at which angles we will observe the corresponding intensity maxima for a given wavelength. This angle has to be large enough in order to separate the scattering event clearly from the primary beam. This is why we need different instruments to study materials on different length scales. Table 5.1 gives two examples.

Example	$d$	$\Delta Q$	$2\theta$ ( $\lambda=1 \text{ \AA}$ )	$2\theta$ ( $\lambda=10 \text{ \AA}$ )	Technique
Distance between atoms in crystals	2 $\text{\AA}$	3.14 $\text{\AA}^{-1}$	29°	"cut-off"	wide angle diffraction
Precipitates in metals (e.g. Co in Cu)	400 $\text{\AA}$	0.016 $\text{\AA}^{-1}$	0.14°	1.46°	small angle scattering

**Tab. 5.1:** Examples for scattering from structures on different characteristic real space length scales  $d$ .  $\Delta Q$  is the corresponding characteristic scattering vector according to (5.14),  $2\theta$  the scattering angle according to (5.13), calculated for two different wavelength  $\lambda$ .

1. The study of structures on atomic length scales is typically done with a wavelength of around 1  $\text{\AA}$  (comparable to the distance between the atoms) and the scattered intensity is observed at rather large angles between 5° and 175°. Therefore one speaks of *wide angle diffraction*, which is employed for the study of atomic structures.
2. For the study of large scale structures (precipitates, magnetic domains, macromolecules in solution or melt) on length scales of 10 up to 10,000  $\text{\AA}$  (1 up to 1000 nm), the magnitude of the relevant scattering vectors as well as the corresponding scattering

angles are small. Therefore one chooses a longer wavelength in order to expand the diffractogram. The suitable technique is *small angle scattering*, which is employed to study large scale structures.

In what follows we will first focus on the study of large scale structures. In the corresponding conceptually very simple instruments, some typical considerations for the design of an instrument can be exemplified. We will distinguish between small angle neutron scattering instruments and reflectometers, discuss the basic instrument concepts and list some possible applications. After having discussed how large scale structures can be studied with neutron diffraction, we will then introduce instruments for wide angle scattering and their possible applications.

### 5.4.2 Small angle neutron scattering SANS

As mentioned in chapter 5.4.1, small angle scattering is employed whenever structures on length scales between typically  $10 \text{ \AA}$  and  $10,000 \text{ \AA}$  ( $1 \text{ nm}$  and  $1,000 \text{ nm}$ ) are of interest. This range of real space lengths corresponds to a scattering vector of magnitude between about  $10^{-1} \text{ \AA}^{-1}$  and  $10^{-4} \text{ \AA}^{-1}$  ( $1 \text{ nm}^{-1}$  and  $10^{-3} \text{ nm}^{-1}$ ). In order to observe the scattering events under reasonable scattering angles, one chooses a rather long wavelength. However, due to the moderator spectrum (see chapter "Neutron Sources"), there is very little neutron flux at wavelengths above  $20 \text{ \AA}$ . Therefore typically neutrons of wavelength between  $5$  and  $15 \text{ \AA}$  are employed for small angle neutron scattering.

Two different principles of small angle neutron scattering will be distinguished in this chapter: the pinhole SANS and the focusing SANS depicted in figures 5.4 and 5.5, respectively. Other types of instruments, e.g. with multi-pinhole grid collimation, are variants of these techniques and will not be discussed here.

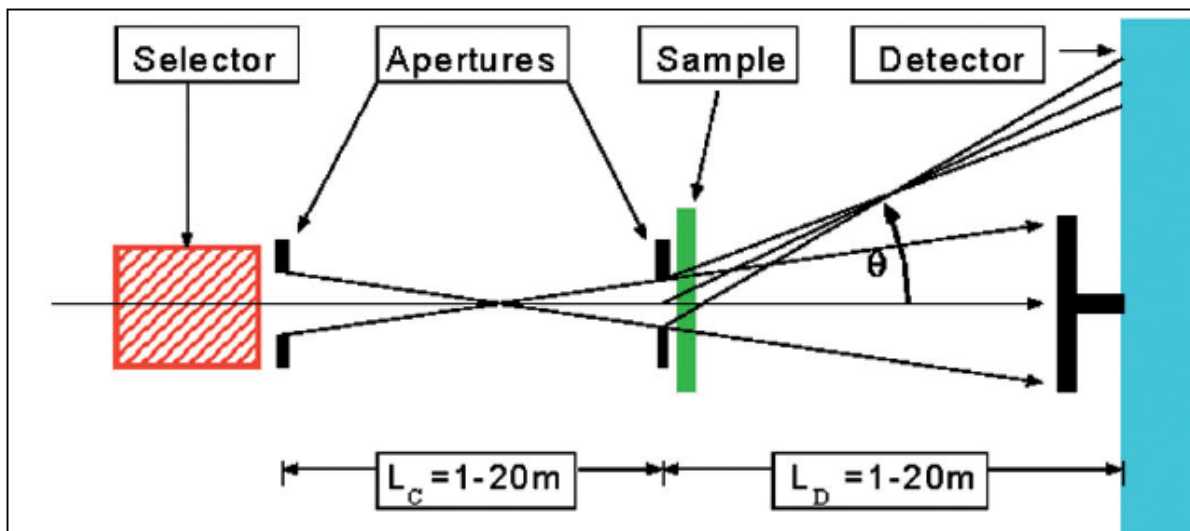


**Fig. 5.4:** Schematics of a pinhole SANS, where the incident wave vector is defined through distant apertures (KWS-1 or KWS-2 of JCNS [3]).

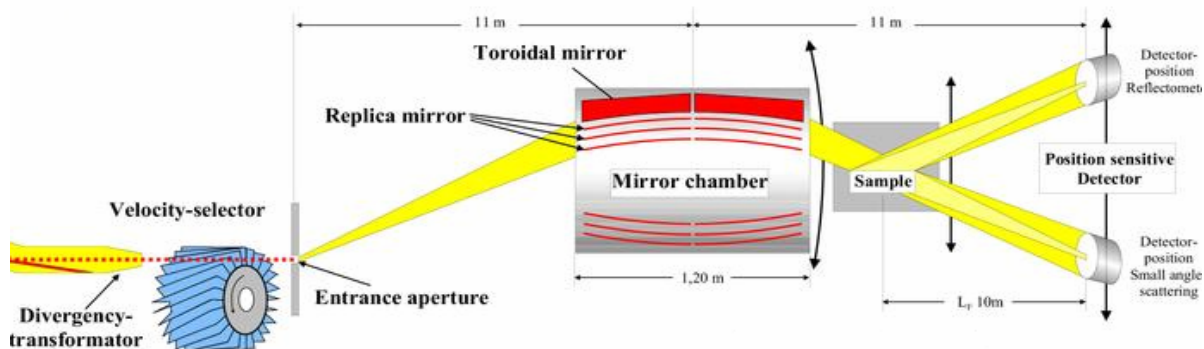


**Fig. 5.5:** Schematics of a focusing SANS, where an image of the entrance aperture is produced on the detector by a focusing mirror (KWS-3 of JCNS [3]).

For both instrument concepts, the wavelength band is usually defined by a so-called velocity selector. Figure 5.6 shows a photo of a velocity selector drum build in Jülich for the instrument KWS-3.



**Fig. 5.6:** Drum of a velocity selector made from a light-weight, neutron absorbing alloy (MgLi). A velocity selector works on the "screw thread principle": it is rotating at high speeds and only neutrons in a certain velocity band can travel undisturbed in the channels between the absorbing partition walls; neutrons outside this velocity band are stopped in the walls. Thus only a certain velocity- or wavelength band can pass this device.

In the pinhole SANS, the incident wave vector  $\underline{k}$  is defined by two distant apertures of comparable size. The longer the distance between the diaphragms, the higher is the collimation for a given cross section of the beam. The sample is placed right next to the second aperture and the scattered neutrons are being recorded in a detector, which is at a large distance from the sample; typically the sample-detector distance is comparable to the collimation distance. The overall length of such an instrument can amount to 40 m, up to 80 m.

In contrast to the pinhole SANS, the focusing SANS uses a divergent incident beam and a focusing optical element produces an image of the entrance aperture on the detector. The sample is positioned directly behind the focusing element. Small angle scattering from the sample appears on the position-sensitive area detector around the primary beam spot. Such a set-up with a focusing element would be the natural solution in light optics, where focusing lenses are readily available. Due to the weak interaction of neutrons with matter, the index of refraction for neutrons is very close to one, and it is difficult to produce efficient focusing elements. In case of the focusing SANS realized by Forschungszentrum Jülich [4], a toroidal<sup>5</sup> mirror is employed as focusing element. Locally, the toroidal shape is a good approximation to an ellipsoid with its well-known focusing properties. The challenge in realizing such a device lies in the fact that small angle scattering from the focusing element has to be avoided i.e.

<sup>5</sup> A torus is a surface of revolution generated by revolving a circle about an axis coplanar with the circle, which does not touch the circle (examples: doughnuts, inner tubes).

the mirror has to be flat on an atomic scale (root-mean square roughness of about 3 Å !), which became possible due to the developments of optical industry for x-ray satellites.<sup>6</sup>

As an example of the considerations leading to the design of a neutron scattering instrument, we will now discuss the resolution of a pinhole SANS machine. In general terms, the resolution of an instrument denotes the smearing out of the signal due to the instruments' finite performance (5.12). As neutron scattering is a flux limited technique, there is need for optimization: the better the resolution of the instrument, i. e. the better the angular collimation  $\Delta\theta$ , the smaller the wavelength spread  $\Delta\lambda$ , the smaller is the intensity recorded on the detector. Therefore resolution has to be relaxed to such an extent that the features of interest are still measurable and not smeared out entirely by the resolution of the instrument, while at the same time the intensity is maximized. In order to determine the resolution of a SANS instrument, we start from (5.13):  $Q = \frac{4\pi}{\lambda} \sin \theta$ . The influence of angular- and wavelength spread can be determined by differentiation of this equation, where the different contributions have to be added quadratically:

$$\begin{aligned} \Delta Q^2 &= \left(\frac{\partial Q}{\partial \theta}\right)^2 (\Delta\theta)^2 + \left(\frac{\partial Q}{\partial \lambda}\right)^2 (\Delta\lambda)^2 = \left(\frac{4\pi}{\lambda}\right)^2 \cos^2 \theta (\Delta\theta)^2 + \left(\frac{4\pi \sin \theta}{\lambda^2}\right)^2 \Delta\lambda^2 \\ &\stackrel{\uparrow}{=} \left(\frac{4\pi}{\lambda}\right)^2 \left[ (\Delta\theta)^2 + \theta^2 \left(\frac{\Delta\lambda}{\lambda}\right)^2 \right] = \frac{k^2}{12} \left[ \left(\frac{d_D}{L_D}\right)^2 + \left(\frac{d_E}{L_C}\right)^2 + \left(\frac{d_S}{L_C} + \frac{d_S}{L_D}\right)^2 + \theta^2 \left(\frac{\Delta\lambda}{\lambda}\right)^2 \right] \end{aligned} \quad (5.15)$$

$\Delta Q^2$  is the variance of the scattering vector due to the finite collimation and monochromatization.  $d_E$  and  $d_S$  are the diameters of the entrance and sample aperture, respectively.  $d_D$  denotes the detector pixel size.  $L_C$  and  $L_D$  are collimation length and sample-detector distance, respectively. An optimization can be achieved, if all terms in (5.15) contribute the same amount, which leads to the condition

$$L_D = L_C, \quad d_E = d_D = 2d_S \quad (5.16)$$

(5.16) shows that a pinhole SANS has to be designed such that sample-to-detector distance  $L_D$  is equal to the collimation length  $L_C$ . Typical values are  $L_D = L_C = 10$  m with openings of  $d_E = 3$  cm for the entrance- and  $d_S = 1.5$  cm for the sample aperture. Note that one can chose the opening of the entrance aperture to be twice as large as the opening of the sample aperture - or sample size - without sacrificing markedly in resolution, while gaining in neutron count rate! The detector needs a minimum pixel resolution  $d_D \approx d_E$ ; A detector with a radius of about  $R_D \approx 30$  cm is necessary to cover the required Q-range up to  $0.05 \text{ \AA}^{-1}$  at  $L_D = 10$  m and for  $\lambda = 8 \text{ \AA}$ . Having defined the incident collimation, we can now determine the appropriate wavelength spread with the same argument as above: the last term in the sum in (5.15), corresponding to the wavelength spread, should contribute the same amount to the variance of the scattering vector as the corresponding terms for the collimation, i. e.:

$$\frac{\Delta\lambda}{\lambda} = \frac{d_E}{L_C} \cdot \frac{L_D}{r_D} \approx \frac{d_E}{r_D} \approx \frac{1}{10} = 10\% \quad (5.17)$$

(5.17) demonstrates that in general for small angle scattering we don't need a very high degree of monochromatization. A 10 % wavelength band is acceptable, since for small angles the smearing due to the wavelength spread is quite comparable to the smearing due to the incident divergence. This is the reason why usually a velocity selector is employed as monochromatizing element for small angle scattering, as it lets a wavelength band of typically 10 % pass.

---

<sup>6</sup> It should be mentioned that nowadays focusing lenses for neutron scattering have also been realised. These have a very long focal distance, but can be employed to improve intensity or resolution in pinhole SANS.

Let us give a short introduction into the analysis of small angle scattering experiments. As in any scattering experiment, the detected intensity is proportional to the scattering cross section, which in the SANS case is usually normalised to the sample volume and therefore has the unit [ $\text{cm}^{-1}$ ]:

$$\frac{d\Sigma}{d\Omega} = \frac{1}{V_{\text{sample}}} \cdot \frac{d\sigma}{d\Omega} \quad (5.18)$$

Here we discuss the so-called “two phase model” only, where homogeneous particles are dispersed in a matrix (e. g. precipitates in metals or nanoparticles in solution etc.). The cross section will then be proportional to the contrast between particles and solution

$$\Delta b = \sum_j b_j (\rho_{j,P} - \rho_{j,M}) \quad (5.19)$$

where  $j$  labels atom species  $j$  of scattering length  $b_j$  with number density  $\rho_{j,P}$  in the particle and  $\rho_{j,M}$  in the matrix, respectively. The differential cross section per particle is given by the interference term (note: we use a continuum description for the small  $Q$  limit):

$$\begin{aligned} \frac{d\Sigma}{d\Omega}(\underline{Q}) &= \left| \int_V \Delta b \cdot e^{i\underline{Q}\cdot\underline{r}} d^3r \right|^2 \\ &= \Delta b^2 V^2 \underbrace{\left| \frac{1}{V} \int_V e^{i\underline{Q}\cdot\underline{r}} d^3r \right|^2}_{f(\underline{Q})} \end{aligned} \quad (5.20)$$

Here  $f(\underline{Q})$  denotes the *particle form factor* for a homogeneous particle of volume  $V$ :

$$f(\underline{Q}) = \frac{1}{V} \int_V e^{i\underline{Q}\cdot\underline{r}} d^3r \quad (5.21)$$

(5.20) is the differential cross section for a single particle. For very dilute solutions of identical particles, the cross section will be given by (5.20) times the number  $N$  of particles (“single particle approximation”). However, in more concentrated solutions, there will be additional interference effects between the particles, which are described by the so-called *structure factor*  $S$  and we obtain the modified cross section for dense solutions:

$$\frac{d\sigma}{d\Omega} = N \cdot \Delta b^2 \cdot V^2 \cdot |f(\underline{Q})|^2 \cdot S(\underline{Q}) \quad (5.22)$$

where  $S(\underline{Q})$  is related to the Fourier Transform of the pair correlation function  $g(\underline{R})$  between the single particles at distance  $\underline{R}$ :

$$S(\underline{Q}) = 1 + \frac{1}{V_{\text{sample}}} \int_{V_{\text{sample}}} g(\underline{R}) e^{i\underline{Q}\cdot\underline{R}} d^3r \quad (5.23)$$

(Note: for vanishing pair correlations  $g(\underline{R}) \equiv 0$ , i. e. random distributed particles, the structure factor has to be unity:  $S(\underline{Q}) \equiv 1$ ).

The isotropic form factor of a homogeneous sphere of radius  $R$  has already been given in the chapter “Neutron Primer”:

$$f(Q) = 3 \frac{\sin QR - QR \cos QR}{(QR)^3} \quad (5.24)$$

For forward scattering  $f(Q=0) = 1$  per definition. For small values of the scattering vector, this expression can be approximated by:

“Guinier Law” for  $QR \leq 2$ :

$$|f(Q)|^2 \approx e^{-\frac{(QR_G)^2}{3}} \approx 1 - \frac{Q^2 R_G^2}{3} \quad (5.25)$$

Here the quantity  $R_G$  is the so-called *radius of gyration* of the particle. For a spherical particle  $R_G^2 = \frac{3}{5} R^2$ , but  $R_G$  can be defined in a more general way also for non-spherical particles.

For  $QR=3$  the form factor squared has dropped to about 10 %. In the larger  $Q$  region - neglecting the sharp minima of the form factor (5.24), which are often not visible due to particle size distribution and instrumental resolution - the form factor follows the behaviour:

“Porod Law” for  $QR \geq 4.5$ :

$$|f(Q)|^2 \approx 2\pi \frac{A}{V^2} Q^{-4} \quad (5.26)$$

where  $A=4\pi R^2$  is the surface, and  $V = \frac{4\pi}{3} R^3$  the volume of the sphere of radius  $R$ . In small angle scattering, often times one does not deal with simple geometrically smooth particles in a second phase. In stochastic growth processes or soft matter system, irregular *fractal* structures can appear, which show self-similarity on multiple length scales. For such structures, power laws with other exponents are observed:

$$\begin{aligned} \frac{d\sigma}{d\Omega} (\text{mass fractal}) &\sim Q^{-D} = Q^{-1} \dots Q^{-3} \\ \frac{d\sigma}{d\Omega} (\text{surface fractal}) &\sim Q^{D_s-6} = Q^{-3} \dots Q^{-4} \end{aligned} \quad (5.27)$$

where  $D$  denotes the so-called *fractal dimension* for porous objects.  $D$  is in general smaller than 3 and non-integer. If the particles have a dense core, but a rough self-similar surface, they are called *surface fractals* with a surface area of  $A \sim R^{D_s}$ . From the above discussion we see that characteristic regions can be distinguished in a small angle scattering experiment:

1. Close to forward direction in the very small  $Q$  limit and for dilute solutions, we observe constant scattering proportional to the number of particles  $N$ , the square of the particle volume  $V^2$  and contrast (5.19). For known contrast, we can deduce the product  $N \cdot V^2$ , if the scattering is measured in absolute units by comparing to a known scatterer e. g. water. For dense solutions, the structure factor form correlations between particles becomes apparent.
2. In the region up to  $QR \leq 2$ , the Guinier Law (5.25) holds for compact particles. From a *Guinier-Plot*  $\ln \frac{d\sigma}{d\Omega}$  versus  $Q^2$  one can determine the radius of gyration

$$R_G = \frac{\int_V r^2 \Delta b(r) d^3 r}{\int_V \Delta b(r) d^3 r} \quad (5.28)$$

3. In the Porod-region  $QR \geq 4.5$

$$\frac{d\sigma}{d\Omega} = \Delta b^2 2\pi N A Q^{-4} \quad (5.29)$$

we can, independent of particle shape, determine the total surface area  $N \cdot A$  of all particles with sharp surfaces from a *Porod Plot*  $\frac{d\sigma}{d\Omega} \cdot Q^4$  versus  $Q^4$ .

4. Finally, if  $Q$  approaches the value  $1/a$  where  $a$  corresponds to typical atomic distances, we approach the region of Bragg scattering from atomic structures (wide angle scattering).

Let us now turn to applications of small angle scattering. One example is given in figure 5.7, which is concerned with the self-organization of crystalline amorphous diblock-copolymers [4]. Combining three different instruments, small angle scattering has been observed over ten orders of magnitude in cross section and nearly four orders of magnitude in momentum transfer. In different regions, different power laws apply, corresponding to different structures observed: the  $Q^{-2}$  power law corresponds to  $2d$  structures on the shortest length scale, the  $Q^{-1}$  power law corresponds to the organization of rods in bundles, while the  $Q^{-3}$  power law corresponds to a network of bundles with a mass fractal aspect and finally, correlations become visible in the very low  $Q$ -range.

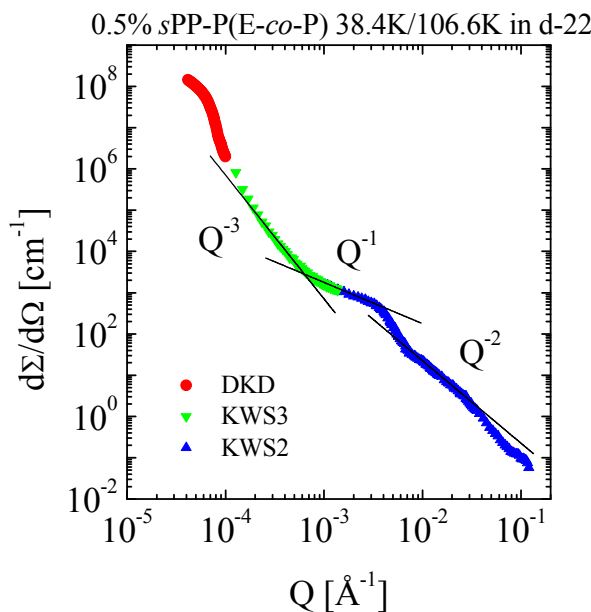


**Fig. 5.7:** SANS investigation of the self-organization of a crystalline-amorphous diblock-copolymer measured with three different instruments of different resolution: double crystal diffractometer, focussing SANS and pinhole SANS for the low, medium and larger  $Q$  range, respectively. Plotted is the cross section in absolute units versus the magnitude of the scattering vector. For details see [4].

We will end this short introduction into the principles of small angle scattering by listing some examples for applications of small angle scattering in different fields of science:

- *soft matter*: polymers and colloids, e. g. micelles, dendrimers, liquid crystals, gels, reaction kinetics of mixed systems, ...
- *materials science*: phase separation in alloys and glasses, morphologies of superalloys, microporosity in ceramics, interfaces and surfaces of catalysts
- *biological macromolecules*: size and shape of proteins, nucleic acids and of macromolecular complexes, biomembranes, drug vectors
- *magnetism*: ferromagnetic correlations and domains, flux line lattices in superconductors, ...

### 5.4.3 Large scale structures: Reflectometry

As elaborated in chapter 5.4.2, neutron small angle scattering is applied to determine large scale structures, e. g. scattering length density fluctuations on length scales of some 100 Å in bulk material. There is another type of instruments, which is dedicated to the study of large scale structures in thin film systems, on surfaces and in multilayers. Such an instrument is called a *neutron reflectometer*. This conceptually simple instrument is depicted schematically in figure 5.8.

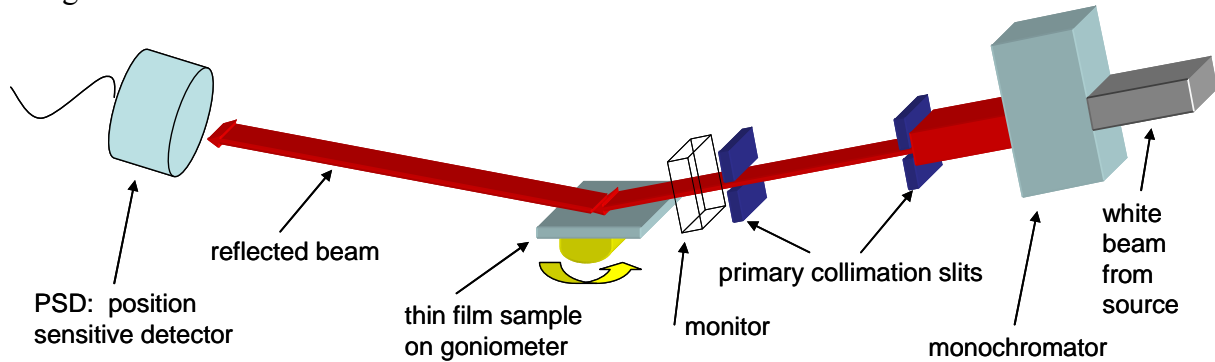


**Fig. 5.8:** *Schematics of a neutron reflectometer. Monochromatization can be done in many different ways: by a velocity selector, by a crystal monochromator, or by a chopper in a time-of-flight instrument. Collimation slits define the direction of the incident beam. The monitor is a low efficient detector of high transmission, which measures the incident flux on the sample. The reflected neutrons are either detected in a position sensitive detector, or a secondary collimation track in front of a point detector selects the direction of the reflected beam. For magnetic samples, a polarizer, a polarization analyzer and guide fields can be inserted for polarization analysis experiments.*

Similar to a pinhole SANS instrument, the incident beam is collimated through a set of two well separated slits. However, since in reflectometry, one is mainly interested in the momentum transfer perpendicular to the planar sample surface, the collimation of a reflectometer is tight only in this direction. Along the sample surface the beam can be wide and have a larger divergence in order to gain intensity. This collimated beam impinges on the sample under a grazing angle (typically fractions of a degree up to a few degrees) and is reflected into a single point detector or a position sensitive detector. To define the angle of exit for a point detector, a secondary collimation is needed between sample and detector. The incident beam is monochromatized using different techniques, depending on the resolution requirements: velocity selector, time-of-flight chopper or crystal monochromator.

With such an instrument, the layer structure of a sample can be determined, such as layer composition, layer thickness and surface- or interfacial roughness. This information is obtained in so-called specular reflection, for which the incident angle is equal to the final angle like in a reflection from a perfect optical mirror. In this case, the momentum transfer of the neutrons is perpendicular to the surface of the sample and thus only laterally averaged information can be obtained. In order to determine lateral correlations within the layers, for example magnetic domain sizes, a momentum transfer within the layer has to occur, which implies that angle of incidence and final angle have to be different. Short range correlation within the layers will then give rise to so-called off specular diffuse scattering as well know in optics from a bad optical mirror.

The scattering geometry is shown in Fig. 5.9.

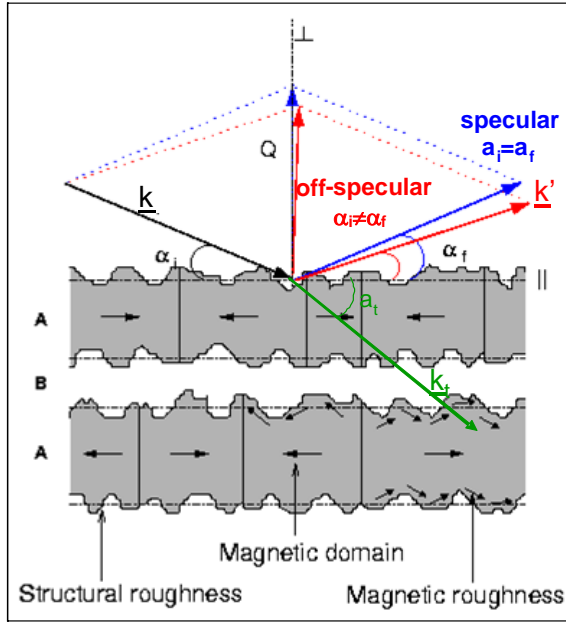


**Fig. 5.9:** Scattering geometry for grazing incidence neutron scattering. Specular reflections are obtained, if the angle of incidence equals the final angle  $\alpha_i = \alpha_f$ . Off-specular scattering is observed at  $\alpha_i \neq \alpha_f$ .

In fact, the theoretical description of neutron reflectometry follows exactly along the lines of conventional optics, except that for neutrons in most cases the index of refraction is smaller than one and thus external total reflection occurs for neutrons coming from vacuum towards matter<sup>7</sup>: The index of refraction  $n$  of neutrons of wavelength  $\lambda$  from a layer composed of elements with scattering length  $b_i$  and number density  $\rho_i$  and linear absorption coefficient  $\mu_n$  is given by:

$$n = 1 - \frac{\lambda^2}{2\pi} \sum_j b_j \rho_j - i \frac{\lambda}{4\pi} \mu_n =: 1 - \delta - i\beta \quad (5.30)$$

Refraction and total reflection are described by the well-known *Snell's Law* of optics:

$$\text{Snells law:} \quad \frac{\cos \alpha_i}{\cos \alpha_t} = \frac{k_t}{k} = n \quad (5.31)$$

$$\text{angle of total reflection:} \quad \cos \theta_c = n \quad (5.32)$$

The intensities of reflected and transmitted beam can be determined from the optical *Fresnel equation* ( $A_0, A_1, B_0$ : amplitudes of incident, transmitted and reflected waves, respectively;  $k_z, k_{tz}$ : component of wavevector  $\underline{k}$  and  $\underline{k}_z$ , respectively, perpendicular to average surface):

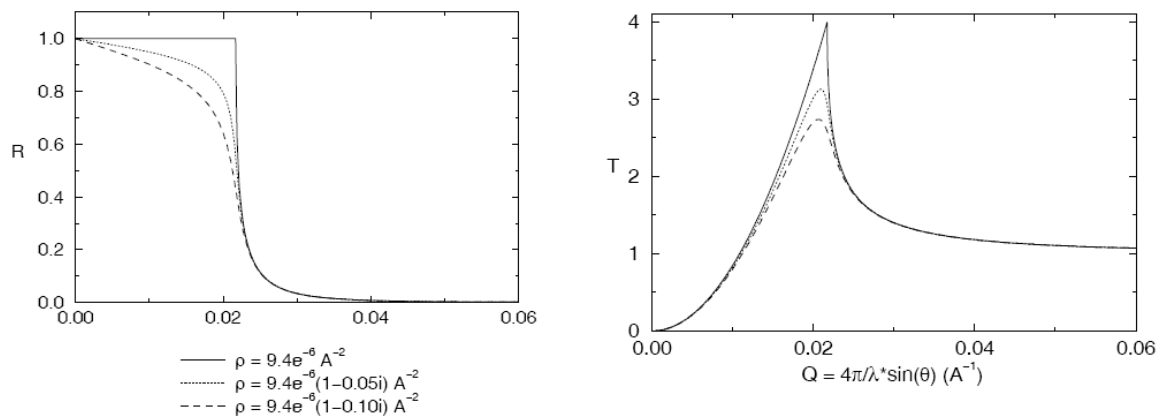
Fresnel equation:

$$\text{Reflectivity } R = \left| \frac{B_0}{A_0} \right|^2 = \left| \frac{k_z - k_{tz}}{k_z + k_{tz}} \right|^2 = \left| \frac{\alpha_i - n \cdot \alpha_t}{\alpha_i + n \cdot \alpha_t} \right|^2 \quad (5.33)$$

$$\text{Transmissivity } T = \left| \frac{A_1}{A_0} \right|^2 = \left| \frac{2k_z}{k_z + k_{tz}} \right|^2 = \left| \frac{2\alpha_i}{\alpha_i + n \cdot \alpha_t} \right|^2 \quad (5.34)$$

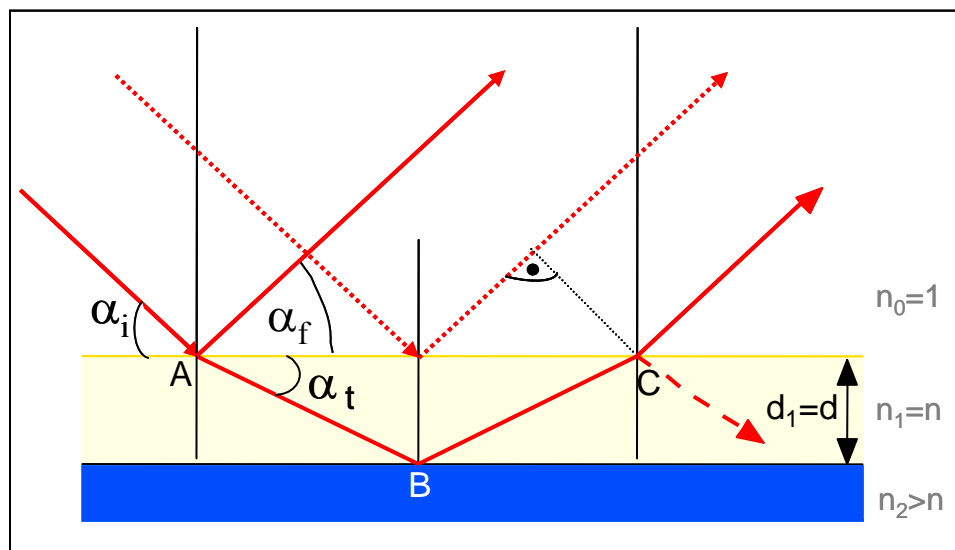
<sup>7</sup> This is exactly what happens in neutron guides, evacuated tubes of usually rectangular cross section, where neutrons are totally reflected from the smooth glass side walls, often coated, e.g. with <sup>58</sup>Ni, to enhance the angle of total reflection. Since for total reflection conditions, reflectivity is close to 100%, neutrons are transported nearly without loss from the source to the instruments by bouncing back- and forth from the guide side walls.

Fig. 5.10 shows as an example the reflectivity and transmissivity of a Ni layer.



**Fig. 5.10:** Reflectivity and transmissivity of neutrons from a Ni surface.

Here we just want to demonstrate with very simple arguments how interference effects from layered structures arise and how the intensity modulation in Q-space are related to real space length scales. Figure 5.11 shows how interference can occur from a beam being reflected at the surface and at the internal interface of a double layer stack.



**Fig. 5.11:** Schematics of the reflection of a neutron beam from a single layer on a substrate. There exists an optical path length difference  $\Delta$  between the rays drawn with a solid line and those drawn with a dotted line.

For simplicity we consider only the case of a specular reflection, i. e. the incident angle  $\alpha_i$  is equal to the angle of exit  $\alpha_f$ :  $\alpha_i = \alpha_f = \alpha$ . Interference occurs between beams reflected from the surface (dotted line in Fig. 5.11) and those first transmitted into the layer, reflected from the interface between layer 1 and substrate and then leaving the layer into vacuum (solid line). To a good approximation, refraction at the top surface can be neglected for incident angles larger than about twice the critical angle of total reflection. In this case  $\alpha_i = \alpha_i = \alpha_f = \alpha$  holds. Since the index of refraction for neutrons is very close to one, this approximation is

valid even for rather small angles of incidence. Then the optical path length difference for the two beams is:

$$\Delta = 2d \sin \alpha \quad (5.35)$$

Here  $d$  is the thickness of the layer 1. We can now determine the distance between interference maxima from the condition that the path length difference has to differ by one wavelength:

$\lambda = 2d \cdot \Delta(\sin \alpha) \approx 2d \cdot \Delta \alpha$ . With  $Q = \frac{4\pi}{\lambda} \sin \alpha \approx \frac{4\pi}{\lambda} \alpha$  we finally obtain:

$$\Delta Q \approx \frac{2\pi}{d} \quad (5.36)$$

Again we can see that the interference phenomena in  $Q$ -space are connected with real space length scales in a reciprocal way. (5.36) tells us that there will be a number of interference maxima at distances in  $Q$  of  $\frac{2\pi}{d}$ . These interference phenomena are called “Kiessig fringes”

and are well known to us in conventional optics for example as the beautiful colors observed in soap bubbles. Figure 5.12 shows as an example the reflectivity of neutrons from a thin nickel layer on a glass substrate, which is nothing else but a section of a neutron guide employed to transport the neutrons from the source to the instrument over long distances by multiple total reflections. The Kiessig fringes are nicely visible in this example and the thickness of the nickel layer can be determined from the distance between adjacent intensity maxima.

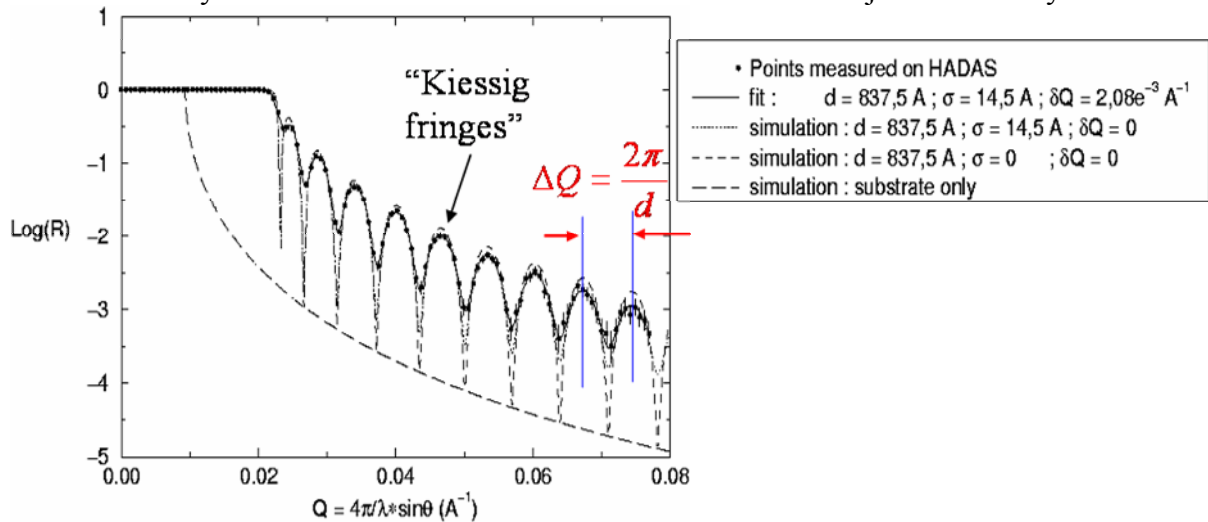


**Fig. 5.12:** Reflectivity of neutrons from a nickel layer on glass substrate on a logarithmic scale. Data points were measured on the HADAS reflectometer of the late FRJ-2 reactor. The solid line shows a fit, where the layer thickness was determined to be 837.5 Å with a root mean square roughness of 14.5 Å and where the resolution of the instrument of  $\delta Q = 2.08 \cdot 10^{-3} \text{ \AA}^{-1}$  has been taken into account; the dotted line shows a simulation for the same structural parameters, but for an ideal instrument without resolution broadening; the short dashed line shows the simulation for the same layer thickness but without roughness; the long dashed line shows the simulation for the glass substrate only.

Neutron reflectometry has many applications in different fields of science of which we can only list a few:

- *soft matter science*: thin films e. g. polymer films; polymer diffusion, self-organization of diblock copolymers; surfactants; liquid-liquid-interfaces, ...
- *life science*: structure of biomembranes

- *materials science*: surface of catalysts; kinetic studies of interface evolution; structure of buried interfaces
- *magnetism*: thin film magnetism e. g. exchange bias, laterally structured systems for magnetic data storage, multilayers of highly correlated electron systems, ...

#### 5.4.4 Atomic structures: Single crystal and powder neutron diffraction

As explained in chapter 5.4.1, wide angle scattering with neutrons of wavelength typically 1 Å is applied for the determination of atomic structures. Due to the periodicity of the lattice, Bragg peaks appear under diffraction angles given by the Bragg equation (compare reflectometry: (5.35) and (5.36)!):

$$2d \sin \theta = \lambda \quad (5.37)$$

The intensity of the Bragg peaks is governed by the arrangement of the atoms within the unit cell (structure factor) and the scattering from the single atom (form factor). By collecting a large set of scattered intensities for many Bragg peaks, modeling the atomic structure and refining the parameters in order to get an optimum agreement between calculated and observed intensities, the arrangement of atoms within the unit cell as well as the arrangements of spins for magnetic samples can be determined. Figure 5.13 shows the schematics of a single crystal diffractometer.

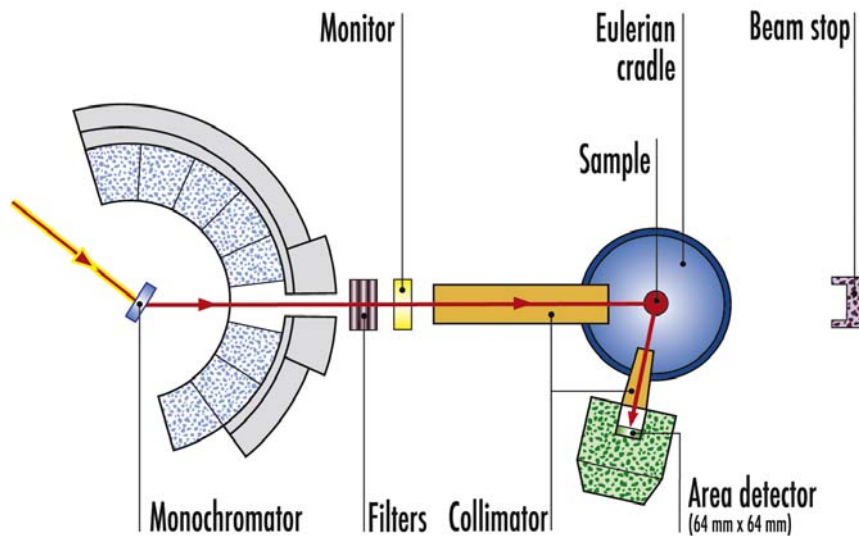


**Fig. 5.13:** *Schematics of a single crystal diffractometer. The drawing shows the layout of the diffractometer D9 at the Institute Laue-Langevin and has been taken from <http://www.ill.eu/>.*

In contrast to small angle scattering, where a broad wavelength band is employed to enhance the scattered intensity, a better monochromatization of typically  $\frac{\Delta\lambda}{\lambda} \sim 1\%$  has to be achieved

for wide angle scattering to avoid the broadening of the Bragg reflections due to the wavelength spread according to (5.37). This monochromatization is typically done by Bragg diffraction from a single crystal. The direction of the incident beam is determined by a set of slits. As Bragg reflections only occur when the corresponding lattice planes have a definite orientation with respect to the incident beam, the single crystal sample is usually mounted on a so-called Eulerian cradle, which allows one to orient the sample using the three Eulerian

angles  $\omega$ ,  $\chi$  and  $\phi$ . Finally the scattered beam is detected in a point- or small area detector. Care must be taken to collect the entire integrated intensity for a scan through the Bragg reflection.

A conceptually simpler experiment for the determination of atomic structures is the neutron powder diffractometer. In this case, since the powder grains in the sample usually have random orientations with respect to the incident beam, there is no need for orienting the sample with respect to the beam. Scattering will always occur for some of the grains, which by chance fulfill the Bragg condition. As scattering occurs for all allowed Bragg reflections simultaneously, it would be very inefficient to detect it by a single point detector, which would have to be positioned recursively for the correct  $2\theta$  values. Therefore in powder diffraction one usually uses a large linear - or even better area - position sensitive detector, which is arranged on a circular arch around the sample position.

While neutron powder diffraction is conceptually simple, it poses the problem that Bragg reflections will overlap for larger unit cells e. g. due to the finite peak width. Among other factors, the peak width is determined by the resolution of the instrument. One can show that the resolution function for a neutron powder diffractometer on a beam being monochromized by a Bragg reflection from a monochromator crystal is given by:

$$(\Delta 2\theta)^2 = U \tan^2 \theta + V \tan \theta + W \quad (5.38)$$

In such a situation, one cannot determine the intensities of the various Bragg reflections separately. The solution to the problem is the so-called *Rietveld*- or profile refinement, where structural parameters (unit cell metric  $a, b, c, \alpha, \beta, \gamma$ , atom positions and site occupations, the Debye-Waller-factors, etc) are refined together with the instrumental parameters (zero point of the scattering angle  $2\theta_0$ , parameters of the resolution function  $U, V, W$ , etc). Assuming a certain peak shape function, this allows one to model the entire powder diffractogram and determine the corresponding parameters from a refinement, which aims at minimizing the weighted sum of the quadratic deviations of calculated and observed intensities for all data points. Figure 5.14 shows an example of such a Rietveld analysis for data taken from a colossal magnetoresistance manganite.

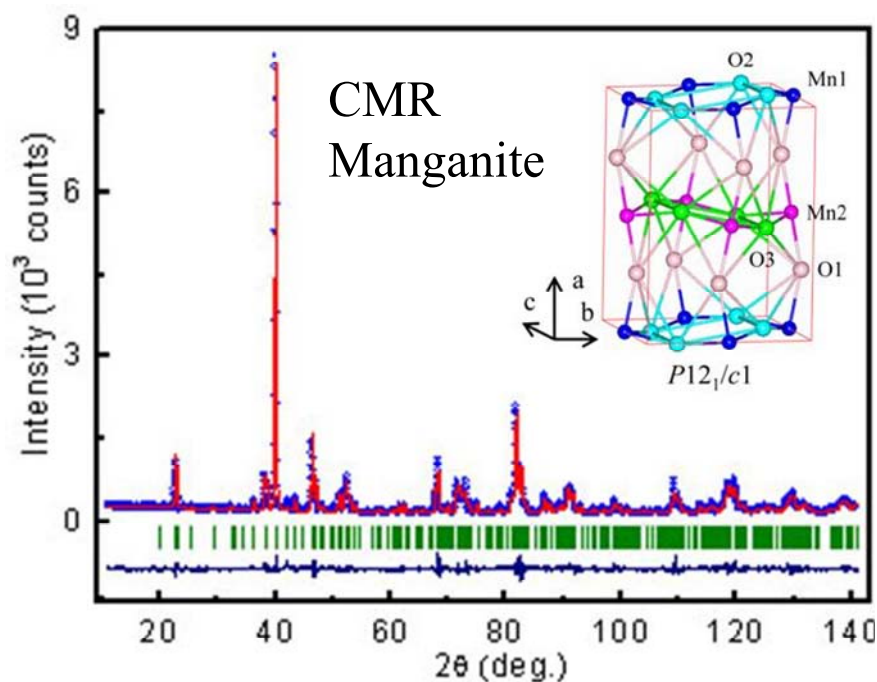


**Fig. 5.14:** Powder neutron diffraction from a colossal magnetoresistance manganite. Points represent the measured intensities, the solid line the calculated profile function. The green bars below the diffractogram indicate the positions of the Bragg reflections and the line beneath shows the difference between observed and calculated intensities [5].

As one can see, there is a very strong overlap of Bragg reflections, especially at larger scattering angles. Still, by using the above mentioned profile refinement technique, the atomic structure of the compound could be determined to a great position.

Applications of wide angle diffractions are manifold:

- *lifescience*: structure of biological macromolecules, e. g. Hydrogen (crystal water!) in protein structures
- *chemistry*: structure determination of new compounds, position of light atoms; time resolved reaction kinetics
- *materials science*: stress-strain determination; texture of materials
- *geo-science*: phase and texture analysis
- *solid state physics*: structure - function relations e. g. in high  $T_C$  superconductors; magnetic structures and spin densities, e. g. in molecular magnets

## 5.5 Spectroscopy

So far, we have only explored the purely elastic - or the quasistatic correlation functions, which give us structural information on various length scales only. We will now turn to the general case of correlation functions in space and time, which allow us to determine in addition the microscopic dynamics of the sample under investigation. Again, different instrument types exist for different applications. First of all, if we consider the neutron as a particle, we can determine the time of flight it needs to travel from the sample to the detector and thus its velocity or energy after the scattering process. With the knowledge of the incident energy, the

energy transfer during the scattering process can be determined. This kind of neutron spectrometer is called a *time-of-flight or TOF spectrometer*. A special case of the TOF spectrometer is the so-called *neutron spin echo spectrometer*, where the time-of-flight of each single neutron is being determined through the Larmor precession of the nuclear spin of the neutron in an external magnetic field. Neutron spin echo spectroscopy has the highest energy resolution and measures the intermediate scattering function directly. Therefore it is well suited to study slow relaxation processes. An alternative approach to spectroscopy is to determine the energy of the scattered neutrons by means of Bragg reflection from an analyzer crystal. Such an instrument is called a *crystal spectrometer* and if the selection of the incident wavelength is done by a crystal monochromator, it is called a *triple axis spectrometer*. A variant of a crystal spectrometer is the high resolution *backscattering spectrometer*. Of course there are various combinations of these techniques, which exist in particular at spallation sources. A discussion of all of the various instrument concepts goes well beyond the scope of this introductory chapter.

### 5.5.1 Time-of-Flight or TOF spectrometry

Figure 5.15 depicts schematically a generic time-of-flight spectrometer.

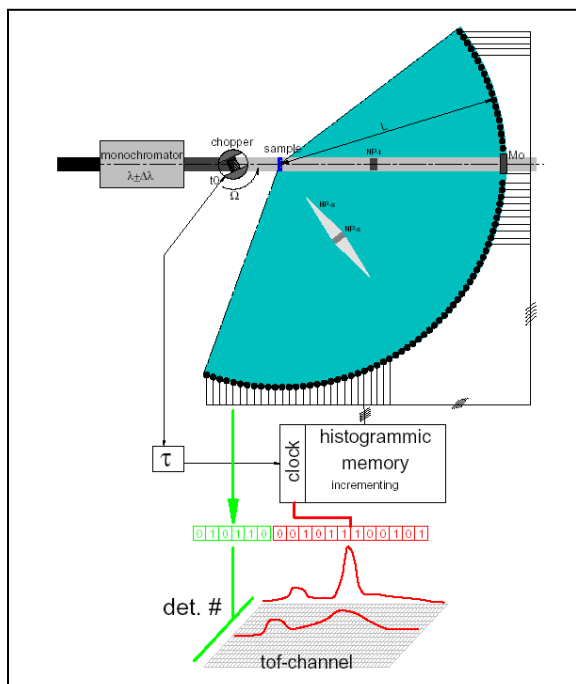


**Fig. 5.15:** *Generic TOF spectrometer. The neutron beam is monochromatized, either by a crystal monochromator (X-TOF) or by time-of-flight (TOF-TOF) with choppers and / or the pulse from a spallation source. A chopper creates monochromatic neutron beam pulses incident on the sample. The scattered neutrons are collected in an array of detectors surrounding the sample. For each detector pixel, the neutrons are counted into a histogram as a function of their arrival time. These intensity – time histograms can be converted into the scattering function  $S(Q, \omega)$  by using a reference sample for absolute calibration and simple kinematic relations between scattering angle and flight time on one hand and scattering vector and energy on the other hand.*

Neutrons are being monochromized either by reflection from a monochromator crystal or by time-of-flight techniques (X-TOF or TOF-TOF instruments). Monochromatic neutron pulses are produced by a chopper, which can be a fast rotating (up to e.g. 600 Hz) disc or drum made from neutron absorbing material, which has a slit that lets neutron pass only during a short time interval of typically some microseconds. This pulsed neutron beam impinges on the sample and is scattered under all possible scattering angles. Neutrons are recorded on a two dimensional position sensitive detector (nowadays, this is often an array of linear position sensitive  $^3\text{He}$  detector tubes) surrounding the sample typically on the surface of a cylinder. From the arrival time of the neutrons in the detector with respect to the starting time given by the opening of the chopper, an intensity spectrum can be recorded for each scattering angle separately as a function of the arrival time of the neutrons in the detector. Using simple kine-

matic equations for the neutron as a particle and a calibration obtained by measuring a reference sample, this time-of-flight spectrum can be converted into the scattering function  $S(Q, \omega)$ . Figure 5.16 illustrates the scattering process in a flight path versus time diagram.

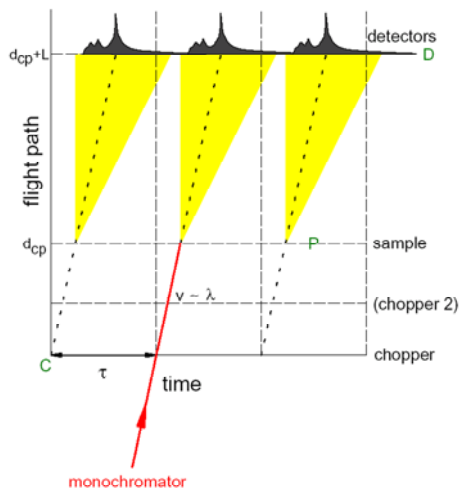


**Fig. 5.16:** Flight-path-versus-time-diagram for a generic time-of-flight instrument (see text). (Courtesy of Dr. M. Monkenbusch)

In such a diagram, a monochromatic neutron beam has a certain slope, which can be derived from the de Broglie equation  $p = \frac{h}{\lambda} = m \cdot v = m \cdot \frac{s}{t}$ :

$$t = \frac{m}{h} \cdot s \cdot \lambda \quad (5.39)$$

Typical velocities for thermal neutrons lie in the range of meter per millisecond. In figure 5.16 the neutrons coming from a monochromator enter the chopper with a certain slope in the path-vs.-time diagram corresponding to the velocity of the monochromatic neutrons. With a repetition rate of  $\frac{1}{\tau}$  given by the chopper frequency, pulses of monochromatic neutrons leave the chopper. A second chopper can be applied to suppress higher order reflections. The neutron scattered from the sample can either gain energy, resulting in a steeper slope in the path-vs.-time diagram or loose energy resulting in a shallower slope. The number of neutrons entering the detector in a certain time interval is counted into a histogram with the elastic line usually being strongest and inelastic events being visible in neutron energy gain or -loss.

A nice example for a powder neutron time-of-flight spectrum is given by the excitation spectrum of a molecular magnet, namely  $Mn_{12}$  acetat, see figure 5.17 [6]. Here the time-of-flight axis has been converted into an energy scale. Clearly visible are nicely separated excitations, which result in the energy level diagram depicted on the middle of figure 5.17. Transitions between these levels correspond to transitions between different values of the magnetic quantum number of the total spin of the molecule. Modeling this energy level spectrum allows one to determine the magnetic interaction parameters, here mainly the magnetic anisotropy.

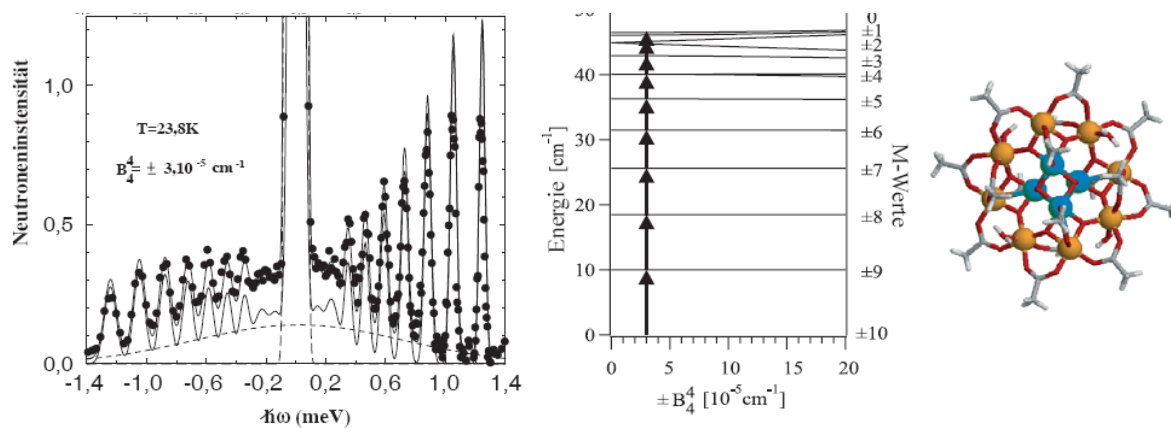


**Fig. 5.17:** *Left:* Time-of-flight spectrum of the molecular magnet  $Mn_{12}$  acetat converted into an energy scale; *middle:* the corresponding energy level diagram; *right:* the magnetic molecule consisting of an outer ring of 8 Mn atoms with parallel coupled spins and an inner ring of 4 Mn atoms with opposite spin orientation. Taken from [6].

Typical applications of time-of-flight spectroscopy can be found in various fields of science:

- *soft matter and biology:* dynamics of gels, proteins and biological membranes; diffusion of liquids, polymers; dynamics in confinement
- *chemistry:* vibrational states in solids and adsorbed molecules on surfaces; rotational tunneling in molecular crystals
- *materials science:* molecular excitations in materials of technological interest (e. g. zeolithes) and especially in diluted systems (matrix isolation); local and long range diffusion in superionic glasses, hydrogen-metal systems, ionic conductors
- *solid state physics:* quantum liquids; crystal field splitting in magnetic systems; spin dynamics in high  $T_C$  superconductors; phase transitions and quantum critical phenomena; phonon density of states.

### 5.5.2 Triple axis spectroscopy

An alternative approach for the study of dynamics of condensed matter systems is the so-called *triple axis spectroscopy*. The schematic of a triple axis spectrometer is depicted in figure 5.18.

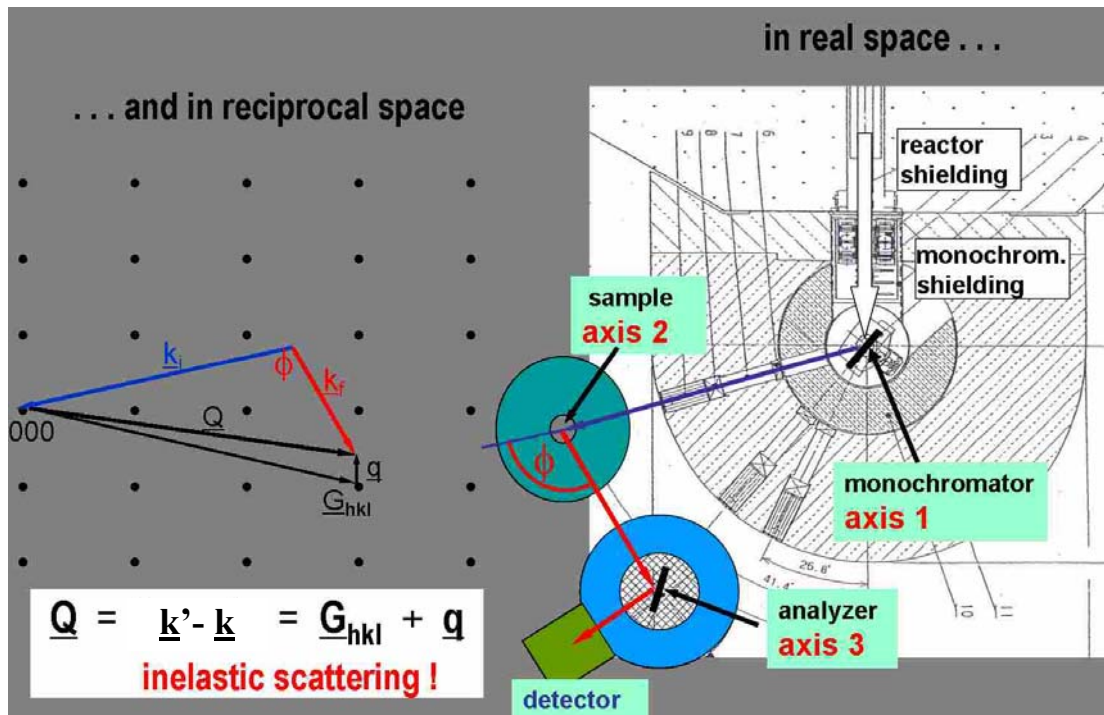


**Fig. 5.18:** *right:* schematics of a triple axis spectrometer showing the three axes; *left:* scattering diagram in reciprocal space. (Courtesy of Dr. H. Conrad)

In this case the energies of the incident and scattered neutrons are selected by means of a single crystal monochromator and - analyzer, respectively. Also the sample is usually in single crystalline form. These crystals (monochromator, sample, analyser) are on rotation tables, which form axis 1, axis 2 and axis 3 of the triple axis spectrometer. If we compare this instrument with the time-of-flight spectrometer shown in figure 5.15, one difference becomes immediately clear: while the time-of-flight spectrometer with its large detector bank allows one to obtain an overview over the excitation spectrum in reciprocal space, the triple axis spectrometer is the instrument of choice, if a certain narrow region in  $\underline{Q}$  and  $\omega$  is of interest. This is the case, if sharp excitations like lattice vibrations (phonons) or spin waves (magnons) are being investigated. A propagation vector of such an excitation together with a certain energy transfer can be selected by setting monochromator, sample and analyzer to the corresponding values as depicted in the scattering diagram of figure 5.18, left. Here the energy

transfer is given by  $\Delta E = \frac{\hbar^2}{2m}(k'^2 - k^2)$ , while the momentum transfer is given as  $\hbar\underline{Q} = \hbar\underline{k}' - \hbar\underline{k} = \hbar\underline{G}_{hkl} + \hbar\underline{q}$ .

Figure 5.19 shows as an example spin wave dispersion relations determined for the garnet  $Fe_2Ca_3Ge_3O_{12}$  by triple axis spectroscopy.

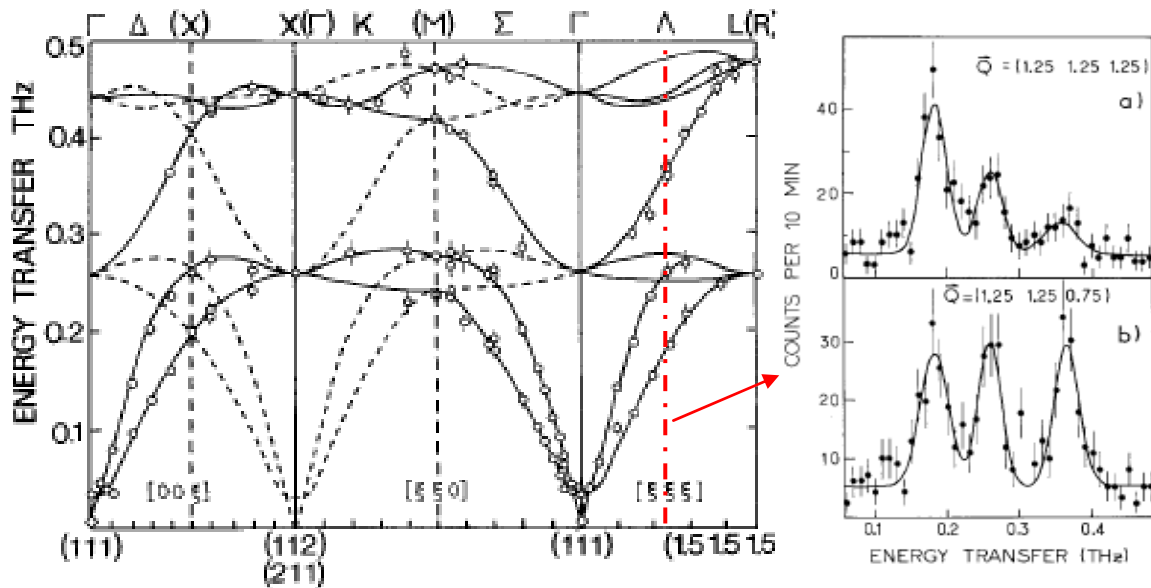


**Fig. 5.19:** Spin wave dispersion relations for the garnet  $\text{Fe}_2\text{Ca}_3\text{Ge}_3\text{O}_{12}$  along main symmetry directions in reciprocal space. The data points are obtained from scans keeping the momentum transfer  $Q$  constant. The figure on the right shows examples of such “constant  $Q$  scans”. The solid lines are model calculations, from which the interaction (exchange) parameters between the spins in the unit cells can be determined; figure taken from [7].

Typical examples of triple axis spectroscopy lie mainly in solid state physics:

- phonon dispersions in crystalline material, from which the interatomic forces can be determined
- spin wave dispersions, which allow one to determine exchange and anisotropy parameters
- dynamics of biological model membranes
- lattice and spin excitations in quantum magnets, superconductors, ...
- phase transitions: critical behavior.

### 5.5.3 High resolution spectroscopy

Both, time-of-flight and triple axis spectroscopy, have typical energy resolutions of a few percent of the incident neutron energy. While such energy resolutions are sufficient in many cases, there is need for higher energy resolutions, for example to investigate the rather slow movements of large macromolecules, the slow spin dynamics of frustrated spin systems, diffusion of atoms or tunneling processes in molecular crystals. In order to improve the energy resolution, one could just narrow the energy band width of the neutrons incident on the sample. However, such an improvement of resolution goes hand-in-hand with the decrease of the signal in the detector and is therefore not practicable. There are, however, alternative approaches to increase the energy resolution: *neutron spin echo spectroscopy* and *backscattering spectroscopy*.

Neutron spin echo spectroscopy can be understood as a further development of the time-of-flight spectroscopy, where the flight time of each single neutron is encoded and thus a broad wavelength band of incident neutron energies can be used. Encoding of the flight-time is done

by the Larmor precession of the nuclear spin of the neutrons in an external magnetic field. Loosely speaking "each neutron carries its own clock" to measure its individual time-of-flight. Figure 5.20 demonstrates the principle of neutron spin echo spectroscopy: the incident neutron beam with a broad wavelength band of typically 10 % is being polarized with the polarization along the neutron flight direction. A so-called  $\frac{\pi}{2}$ -flipper turns the neutron polarization into the vertical direction, just before the neutrons enter a strong magnetic field, which is designed in such a way that the field integral  $\int \underline{B}(\underline{s})d\underline{s}$  is identical for all neutron flight paths (an absolute non-trivial requirement!!). In the external field, the nuclear magnetic moment of the neutron starts to precess in this field with a Larmor precession frequency determined by:

$$\frac{d\underline{s}}{dt} = \gamma \underline{s} \times \underline{B} \quad (5.40)$$

Due to the different neutron velocities and thus different flight times in the magnetic field area, the neutron beam reaching the sample is entirely depolarized. Typical field integrals are in the range of  $0.5 T \cdot m$  giving rise to some 10,000 precessions of the neutron spin. At the sample, the polarization of each neutron is inverted by a so-called  $\pi$ -flipper. In the second arm of the neutron spin echo spectrometer, the scattered neutrons travel through an identical solenoid as on the incident side. If the neutrons are scattered elastically and the field integrals in the two coils are precisely identical, then the full polarization of the neutron beam will be restored and a full intensity will be recorded in the detector after a further  $\frac{\pi}{2}$  flip and a polarization analyzer. This maximum intensity is called the spin echo. This spin echo is due to the fact that in the second coil, each neutron performs as many revolutions as in the first coil and thus has to end up with the initial spin direction. If an inelastic scattering event happens at the sample, the spin echo will be destroyed i. e. the intensity in the detector will be lowered. The echo signal can be measured by scanning the field of the second coil with respect to the field of the first coil. Since the echo signal depends directly on the time-of-flight which neutrons need to travel through the magnetic field region, the spin echo technique directly measures the intermediate scattering function  $S(\underline{Q}, t)$  instead of  $S(\underline{Q}, \omega)$ . This type of spectroscopy is therefore well suited to measure slow relaxation processes like the magnetization dynamics in spin glasses or the dynamics of large macromolecules. This aspect will be detailed in the lecture "Dynamics of Macromolecules".

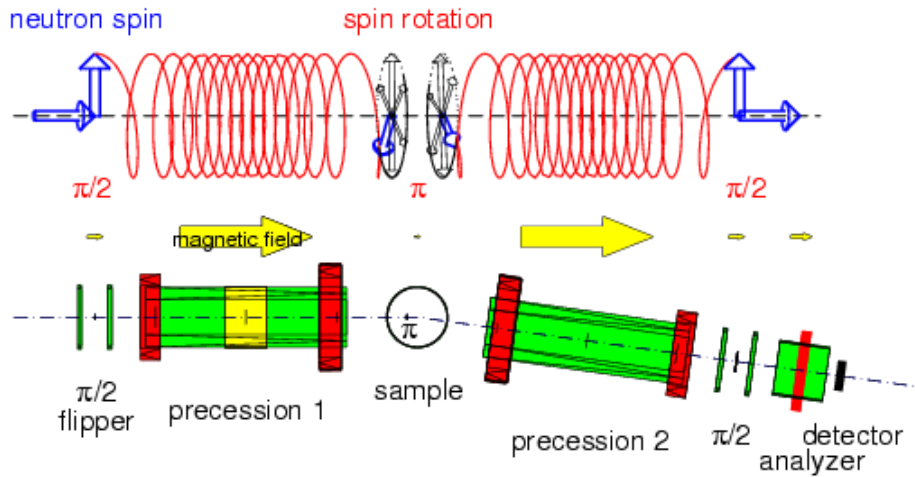


**Fig. 5.20:** Schematics of the neutron spin echo spectrometer of JCNS at the FRM II reactor in Munich [3]. The incident neutron beam has wavelength – or energy band of  $\Delta\lambda/\lambda = 10\%$ .

Another instrument for high resolution spectroscopy, based on a crystal analyzer and thus related to the triple axis spectrometer, is the so-called neutron *backscattering instrument*. Starting from the Bragg equation  $\lambda = 2d \sin \theta$  one can derive the wavelength spread of a Bragg reflection from a monochromator or analyzer crystal by simple derivation:

$$\Delta\lambda = \left(\frac{\partial\lambda}{\partial d}\right)^2 (\Delta d)^2 + \left(\frac{\partial\lambda}{\partial\theta}\right)^2 (\Delta\theta)^2 \Rightarrow \left(\frac{\Delta\lambda}{\lambda}\right)^2 = \left(\frac{\Delta d}{d}\right)^2 + \cot^2 \theta \cdot (\Delta\theta)^2 \quad (5.41)$$

(5.41) shows that the wavelength spread results from two factors: an uncertainty in the lattice d-spacing, which can be minimized for perfect crystals such as silicon or germanium and a term resulting from the divergence of the beam. For backscattering i. e.  $2\theta = 180^\circ$  or  $\theta = 90^\circ$  this latter contribution vanishes due to the  $\cot(\theta)$  dependence. Thus in backscattering, one can work with a very divergent beam and still achieve a very good wavelength- or energy- resolution – of course at the prize of a poor  $Q$  resolution. This principle is applied for backscattering instruments. An example of such a spectrometer from a neutron spallation source is shown in figure 5.21.

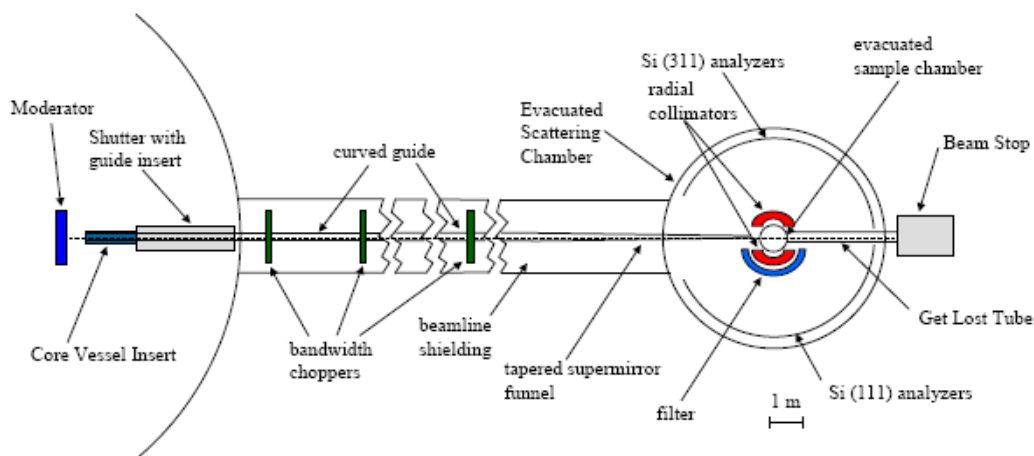


**Fig. 5.21:** Schematics of the neutron backscattering spectrometer BASIS at the Spallation Neutron Source SNS in Oak Ridge, USA, taken from [8].

Neutron pulses are produced in the supercritical hydrogen moderator. These pulses have a width of about  $45 \mu\text{s}$  for  $\lambda = 6.267 \text{ \AA}$  wavelength neutrons (this wavelength corresponds with silicon (111) backscattering analyzer). Bandwidth choppers are used to select a certain wavelength band from the pulsed white neutron beam. A long incident flight path of  $84 \text{ m}$  between moderator and sample allows one to define with great precision the wavelength of the incident neutrons arriving at the sample at a certain time after the initial neutron pulse. Neutrons are scattered from the sample onto *Si* (111) analyzers, reflected from these analyzers into detectors in a close-to-backscattering geometry. In this way the final neutron wavelength is fixed to  $6.267 \text{ \AA}$ , while the incident neutron wavelength varies with time after the pulse and thus the energy transfer can be determined like in a time-of-flight instrument. An energy resolution of about  $2.2 \mu\text{eV}$  can be achieved with the dynamic range of  $\pm 250 \mu\text{eV}$ . Typical applications of such a backscattering spectrometer lie in the investigation of tunneling in molecular crystals, spin diffusion or slow spin relaxation in frustrated spin systems, or atomic diffusion processes.

## 5.12 Summary and conclusions

In this chapter we have given a rough overview over the different neutron scattering techniques and their applications. Many details will be discussed in the practical part of this course. In addition to the instrument concepts presented, there are many variants, which could not be discussed within the scope of this introduction. Besides neutron scattering there are of course many other techniques, which cover similar length and time scales for research in condensed matter. All these techniques are complementary since all of them can only access a certain range of length or time scales and since the contrast mechanisms are quite different for the different techniques. Figures 5.22 and 5.23 depict the relevant length and time scales accessible with the various neutron- and non-neutron techniques.

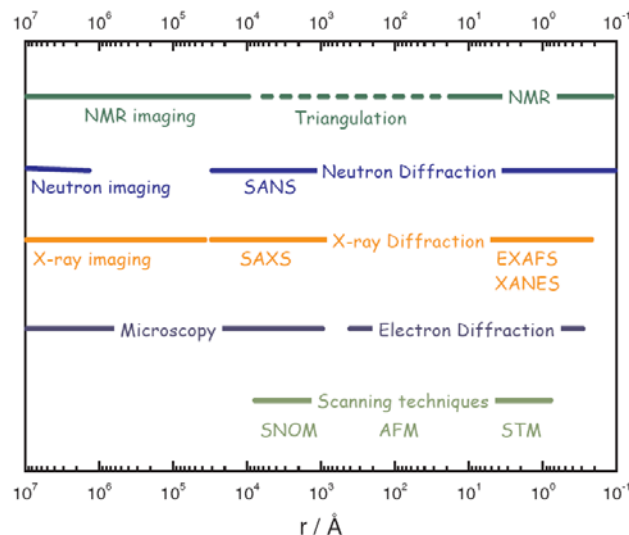


**Fig. 5.22:** *Experimental techniques with spatial resolution: neutron diffraction compared to other experimental techniques; taken from [9].*

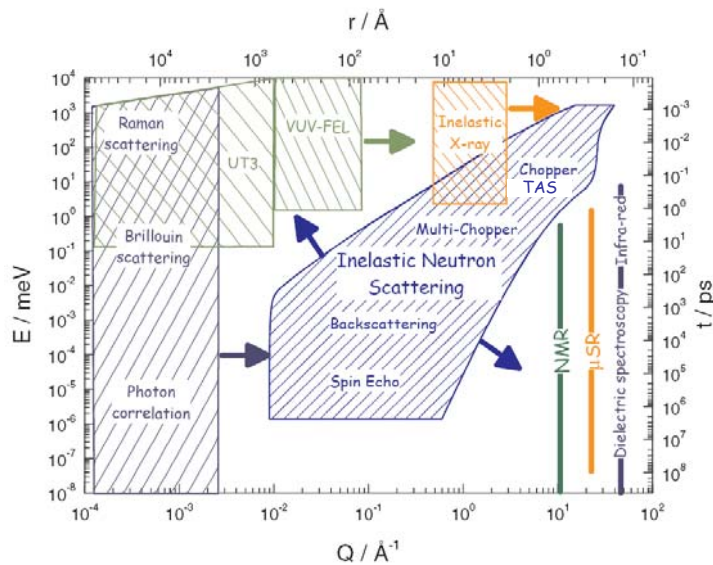


**Fig. 5.23:** *Experimental techniques with time and energy resolution, respectively: neutron spectroscopy compared to other experimental techniques; taken from [9].*

As these figures clearly demonstrate, neutron techniques cover a very large range of length and time scales relevant for research on condensed matter systems. Together with the typical assets of neutrons - sensitivity to magnetism, gentle non-destructive probe, sensitivity to light elements, contrast for neighboring elements etc. - it is clear why neutrons are such an important probe in many fields of research. Figure 5.24 shows how research with neutrons is relevant in many areas of fundamental research and how this in turn is highly relevant for many developments of modern technologies, which are the basis to solve current challenges of mankind.

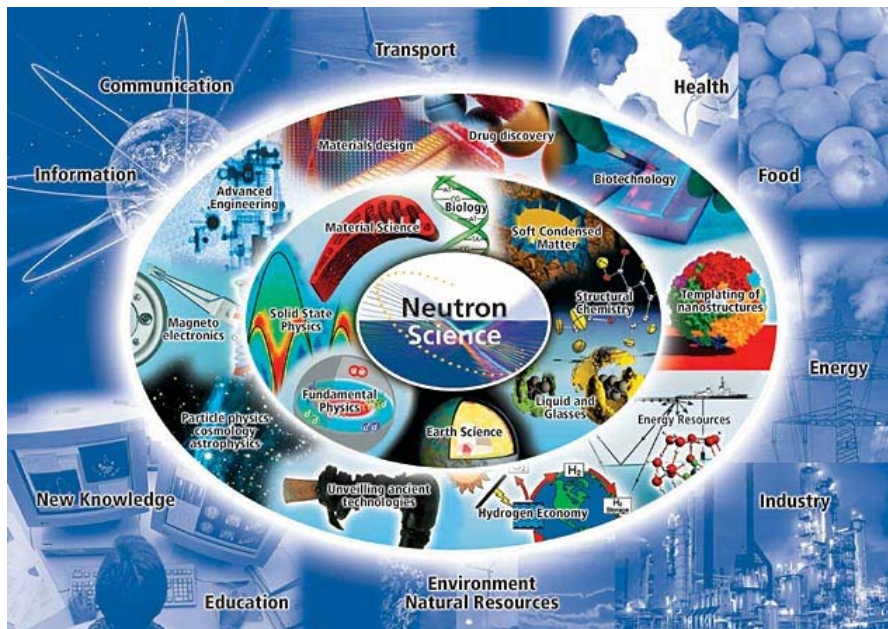


**Fig. 5.24:** *Significance of research with neutrons in fundamental research and modern technologies, which finally shape our environment and help solve pressing problems of modern societies, like energy supply, transport or communication; taken from [9].*

## References:

- [1] Th. Brückel (Ed.) *Forschung mit Neutronen in Deutschland - Status und Perspektiven* Brochure of the German Committee for Research with Neutrons KFN; 2005  
see also <http://www.neutronenforschung.de>
- [2] G.L. Squires *Introduction to the Theory of Thermal Neutron Scattering* Dover Publications Inc.; Reprint 1997  
or  
S.W. Lovesey *Theory of Neutron Scattering from Condensed Matter: Vol. 1 & 2* (International Series of Monographs of Physics) Clarendon Press; 1986
- [3] [http://www.jcms.info/jcms\\_instruments/](http://www.jcms.info/jcms_instruments/)
- [4] A. Radulescu, E. Kentzinger, J. Stellbrink, L. Dohmen, B. Alefeld, U. Rücker, M. Heiderich, D. Schwahn, Th. Brückel, D. Richter; *KWS-3: The New (Very) Small-Angle Neutron Scattering Instrument Based on Focusing-Mirror-Optics*; *Neutron News* **16** (2005), 18 - 21
- [5] H. F. Li, Y. Su, Y. Xiao, J. Perßon, P. Meuffels, Th. Brückel; “*Crystal and Magnetic Structure of Single Crystal  $La_{1-x}Sr_xMnO_3$  ( $x \sim 1/8$ )*”; *European Physical Journal B* **67** (2009), 149 - 157
- [6] R. Bircher, G. Chaboussant, A. Sieber, H.U. Güdel and H. Mutka; *Transverse magnetic anisotropy in  $Mn_{12}$  acetate: Direct determination by inelastic neutron scattering*; *Phys. Rev. B* **70** (2004), 212413-6
- [7] Th. Brückel, B. Dorner, A. Gukasov, V. Plakhty, W. Prandl, E. Shender, O. Smirnow; *Dynamical interaction of antiferromagnetic subsystems: a neutron scattering study of the spinwave spectrum of the garnet  $Fe_2Ca_3(GeO_4)_3$* ; *Z. Phys. B* **72** (1988), 477 - 485
- [8] <http://neutrons.ornl.gov/> ;  
[http://neutrons.ornl.gov/instrument\\_systems/beamline\\_02\\_basis/index.shtml](http://neutrons.ornl.gov/instrument_systems/beamline_02_basis/index.shtml)
- [9] ESS project reports 2003 and update 2004;  
[http://neutron.neutron-eu.net/n\\_documentation/n\\_reports/n\\_ess\\_reports\\_and\\_more](http://neutron.neutron-eu.net/n_documentation/n_reports/n_ess_reports_and_more)